VALIDATION OF DIFFUSION TENSOR IMAGING IN THE CENTRAL

NERVOUS SYTEM USING LIGHT MICROSCOPY

By

Ann Sunah Choe

Dissertation

Submitted to the Faculty of the

Graduate School of Vanderbilt University

in partial fulfillment of the requirements

for the degree of

DOCTOR OF PHILOSOPHY

in

Biomedical Engineering

December, 2010

Nashville, Tennessee

Approved:

Professor Adam W. Anderson

Professor Malcolm J. Avison

Professor Mark D. Does

Professor John C. Gore

Professor Iwona Stepniewska

To my father, In Seong Choe, and mother, Seong Meen Kim,

for their support and love

and

To my brother, TJ Choe, for teaching me that life isn't always sweet,

but love prevails

아빠, 엄마, 그리고 재영이, 모두 너무 사랑해~

ACKNOWLEDGEMENT

TABLE OF CONTENTS

LIST OF TABLES

LIST OF FIGURES

LIST OF ABBREVIATIONS

2D	Two dimensional
3D	Three dimensional
ABA	Adaptive bases algorithm
CC	Correlation coefficient
CNR	Contrast to noise ratio
CNS	Central nervous system
CT	Computed tomography
DTI	Diffusion tensor imaging
DMRI	Diffusion magnetic resonance imaging
DSI	Diffusion spectrum imaging
FA	Fractional anisotropy
fMRI	Functional magnetic resonance imaging
FOD	Fiber orientation distribution
FOV	Field of view
HARDI	High angular resolution diffusion imaging
ICP	Iterative closest point
MD	Mean diffusivity
MI	Mutual information
MRI	Magnetic resonance imaging
NMR	Nuclear magnetic resonance
PBS	Phosphate buffered saline

PET	Positron emission tomography
PGSE	Pulsed gradient spin echo
PPD	Preservation of principal direction
PV	Partial volume
QSI	Q-space imaging
RA	Relative anisotropy
RF	radio frequency
ROI	Region of interest
SNR	Signal to noise ratio
T2-w	T2 weighted
TE	Echo time
TPS	Thin plate spline
TR	Repetition time

LIST OF SYMBOLS

a	Regularization parameter
A_I	Anisotropy index
β	Slope of weighting function
C	Threshold parameter
δ	Diffusion gradient duration
Δ	Diffusion time
$\underline{D}$	Diffusion tensor
$\vec{e}$	Eigenvector
f_r	Normalized radial frequency
f_H	Upper cutoff frequency
f_L	Lower cutoff frequency
G	Gradient strength
λ	Eigenvalue
$\bar{\lambda}$	Mean diffusivity
p	Order of highpass filter
ρ	Standard deviation
q	Order of lowpass filter
ϕ	Azimuthal angle
ϕ_x, ϕ_y, ϕ_z	Rotation around x, y, and z axes
s_x, s_y, s_z	Scaling in x, y, and z directions
θ	Polar angle, Angle of the Fourier transform sample

$\theta_\circ$	Central angle of the desired angle band
t	Iteration time
t_x, t_y, t_z	Translation in x, y, and z plane
T	Smoothing structural tensor
T_I	Intensity gradient tensor
$Tr(\underline{D})$	Trace

CHAPTER I

INTRODUCTION

Complex central nervous system structures such as fiber bundles restrict and define the Brownian motion of the tissue water within. This results in characteristic displacement distribution patterns, which can be measured using diffusion tensor imaging (DTI). Appropriate analysis of the data then can be used to deduce the embedded structural information (1-3). The ability of DTI to probe diffusivity on microscopic scales and the structural information that can be inferred from the diffusivity make the method advantageous for studies of axonal integrity and connectivity. As the number of DTI related investigations has grown and it has become a valuable diagnostic tool (4,5), the need to validate DTI has grown also (6). Although the magnitudes of diffusion coefficients in a fixed brain decrease, it has recently been reported that the diffusion anisotropy is similar to that of a non-fixed brain (7). This finding simplifies a direct comparison of fiber directionality and distribution measured using DTI data with that of fixed, myelin stained brain sections. In an effort to validate the structural information from DTI on a microscopic level, we used a multi-step registration scheme to correlate fiber geometry information from DTI with high magnification light microscopy in non-human primates.

CHAPTER II

BACKGROUND

Diffusion Tensor Imaging

The anatomical structures and functional relationships of the central nervous system (CNS) have been extensively studied using methods such as histology, computer tomography, magnetic resonance imaging, electrophysiology, and other methods not listed here, yet the detailed workings of the CNS are still unknown. One of the biggest challenges in studying the human CNS is obtaining *in vivo* information, due to its structural complexity and the risk of invasive data acquisition. The field of neuroimaging has advanced tremendously over the years in response in areas such as nuclear medicine, computed tomography (CT), functional magnetic resonance imaging (fMRI), and DTI. The focus of this study is DTI, which is the only method available to date that provides microscopic characterization of tissue structure non-invasively.

The intricate assembly of neurons, synapses, and fiber bundles within the CNS provides a unique environment to the tissue water within. The structures restrict and define the Brownian motion of tissue water, and the extent of its movement, characterized by its diffusivity, reflects this environment. DTI measures the characteristic displacement of tissue water, which can be analyzed to deduce tissue structural information (1-3). Background on DTI and other related topics are briefly reviewed in this section.

DTI history

In the early 1950's, the effect of molecular diffusion on the nuclear magnetic resonance (NMR) signal was first observed, most notably by Hahn during spin echo sequence development (8). The pulse sequence was later modified by Carr and Purcell (9) to further investigate the effects of diffusion on NMR signals. Stejskal and Tanner later developed a more stable sequence called the pulsed gradient spin echo (PGSE) sequence (10), which encoded diffusion using strong magnetic field gradient pulses. Various diffusion-encoding pulse sequences as well as different data analysis techniques and parameters such as diffusion coefficient mapping (11) and diffusion tensor mapping have been developed. In particular, the definition of the diffusion tensor was formalized in the early 1990s (12) and lead to the development of the field of DTI. The number of investigations related to DTI and clinical applications of DTI such as stroke (4,5) and schizophrenia (13) has grown rapidly since.

Biological and Physical Basis of DTI

The random movement of microscopic particles suspended in a fluid medium is caused by collisions of the particles with each other and the surrounding medium, and this movement is called Brownian motion (14). During their random walks, the molecules probe their microscopic environment. Measurement and analysis of the molecular movements of water can then be used to infer tissue microstructure in the region (15).

In DTI, signal attenuation is dependent on the diffusion tensor $\underline{D}$ (12) and b-factor. The b-factor reflects the characteristics of gradient pulses used during image

acquisition, such as the gradient amplitude, pulse timing, and shape (15). The diffusion

tensor $\underline{D}$ has components

$$\underline{D} = \begin{bmatrix} D_{xx} & D_{xy} & D_{xz} \\ D_{yz} & D_{yy} & D_{yz} \\ D_{zx} & D_{zy} & D_{zz} \end{bmatrix}. \tag{1}$$

The components represent the second moments of displacement relative to the x, y, and z

axes e.g., $D_{xy} = \dfrac{<x \cdot y>}{2\Delta}$, where Δ is the diffusion time and $<x \cdot y>$ is the expectation

value of the product $x \cdot y$ taken over all observable molecules. Because the principal

axes of tensors (which by hypothesis are the fiber axes) and the gradient x, y, and z axes

often do not coincide, one must account for the coupling of non-diagonal elements of the

b-matrix with those of $\underline{D}$. The process of diagonalization is therefore used to calculate

the eigenvectors, $\vec{e}_1, \vec{e}_2, \vec{e}_3$ and eigenvalues, $\lambda_1, \lambda_2, \lambda_3$ of the tensor.

Data Acquisition

The most commonly used pulse sequence for diffusion magnetic resonance

imaging (DMRI) is the PGSE sequence. The sequences shown in Figure 1.
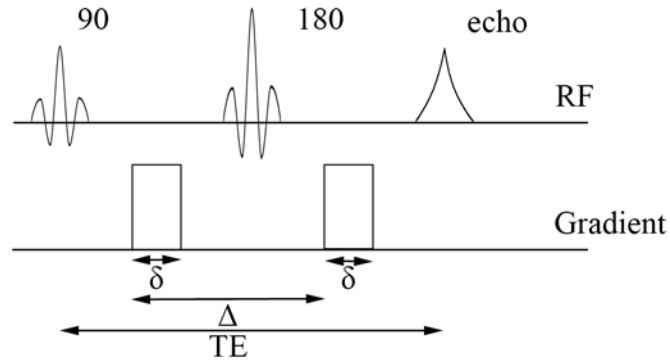
Figure 1. PGSE pulse sequence. Diffusion gradients with amplitude G and duration δ are applied before and after the 180 degree refocusing pulse, separated by time Δ.

The field gradient strength of the PGSE sequence is reduced to zero during the radio frequency (RF) pulses and echoes. This reduction of field gradient strength narrows the linewidth and does not decrease the width of the echoes. The PGSE sequence also provides the means to precisely control the length of time over which diffusion is measured (Δ) by applying a diffusion gradient pulse on both sides of the 180 degree refocusing pulse, as shown in Figure 1. The first pulse is used to encode the initial spin position, and the second pulse detects the incomplete refocusing of spins due to diffusion, if any exists.

Strong diffusion weighing increases echo time (TE), during which a significant signal loss occurs due to T_2 relaxation. This in turn results in an undesirable decrease of signal to noise ratio (SNR). The inherently low SNR may result in subsequent overestimation of diffusion anisotropy and increased uncertainty in tensors (16). One of the approaches to addressing the issue is anisotropic smoothing proposed, by Ding *et al* (17). The algorithm smoothes flow-like structures within images while preserving

structures' edge information. The smoothing algorithm is based on the partial differential equation proposed by Weickert (18):

$$\frac{\partial I}{\partial t} = div(T \cdot \nabla I).$$

(2)

In this relation I is image intensity, ∇I is the intensity gradient, t is the iteration time parameter, and T is the smoothing structural tensor (17) constructed from the intensity gradient tensor T_I,

$$T_I = K_\rho * (\nabla I \otimes \nabla I),$$

(3)

where K_ρ is the Gaussian kernel and ρ is its standard deviation (SD). New eigenvalues are calculated such that:

$$
\begin{aligned}
\lambda_1 &= a, \\
\lambda_2 &= a, \\
\lambda_3 &= a + (1-a)e^{-\frac{C}{A_I}},
\end{aligned}
$$

(4)

where A_I is an anisotropy index of G, a is a regularization parameter, and C is a threshold parameter.

Data Analysis

A few of the most commonly derived diffusion parameters from a tensor are trace ($Tr(\underline{D})$), relative anisotropy (RA), and fractional anisotropy (FA) (16). These parameters are used to quantify the information measured by DTI. They are defined as:

$$Tr(D) = \lambda_1 + \lambda_2 + \lambda_3, \tag{5}$$

$$RA = \sqrt{\frac{(\lambda_1 - \bar{\lambda})^2 + (\lambda_2 - \bar{\lambda})^2 + (\lambda_3 - \bar{\lambda})^2}{3\bar{\lambda}}}, \tag{6}$$

and

$$FA = \sqrt{\frac{3[(\lambda_1 - \bar{\lambda})^2 + (\lambda_2 - \bar{\lambda})^2 + (\lambda_3 - \bar{\lambda})^2]}{2(\lambda_1^2 + \lambda_2^2 + \lambda_3^2)}}, \tag{7}$$

where the mean diffusivity $\bar{\lambda}$ is defined as the average of eigenvalues such that

$$\bar{\lambda} = \frac{\lambda_1 + \lambda_2 + \lambda_3}{3}. \tag{8}$$

$Tr(\underline{D})$ and $\bar{\lambda}$ characterize the displacement of molecules averaged over all directions, while RA and FA characterize the degree of anisotropy. Note that the parameters use all three eigenvalues and therefore represent diffusion characteristics that are independent of reference frame orientation.

Diffusion tensors are inherently three-dimensional (3D) and a proper graphical representation is essential for their characterization. The diffusion ellipsoid (19) is one of the most widely used graphical representations. In this method eigenvalues are used to construct an ellipsoid such that

$$\frac{x'^2}{(2\lambda_1\Delta)} + \frac{y'^2}{(2\lambda_2\Delta)} + \frac{z'^2}{(2\lambda_3\Delta)} = 1 \tag{9}$$

,

where x', y', and z' refer to the principal frame of diffusion tensors. Eigenvectors are represented by the major axes of an ellipsoid and eigenvalues are represented by the length of the axes, as illustrated in Figure 2.
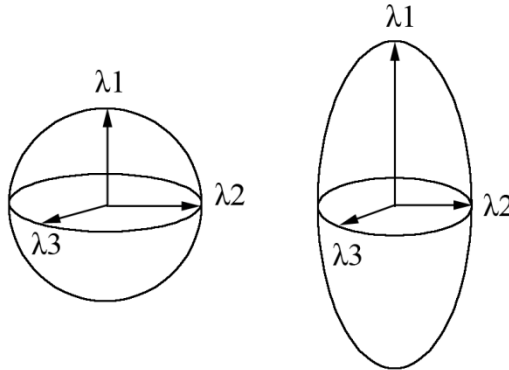
Figure 2. Diffusion ellipsoids. When diffusion is isotropic, the ellipsoids become spherical, displaying equal diffusion displacement in all directions (left). When diffusion is strongly anisotropic, the ellipsoid becomes elongated in the fast diffusion direction.

A parameterized surface representation is another commonly used visualization method. In this method, a tensor is rendered as a surface for which the distance between the origin and the surface in each direction is proportional to the water diffusivity in that

8

direction. This representation, illustrated in Figure 3, employs the equation given by Thorp (20), which is defined as

$$r(\theta,\phi) = (D(\theta,\phi)\sin(\theta)\cos(\phi), D(\theta,\phi)\sin(\theta)\sin(\phi), D(\theta,\phi)\cos(\theta)), \qquad (10)$$

where θ is polar angle and ϕ is azimuthal angle. The parameterized surface representation can also be used to visualize data acquired using high angular resolution diffusion imaging (HARDI) (21), where multiple diffusion weighting gradients are applied in an evenly distributed fashion on the unit sphere to encode complex diffusion. The parameterized surface representation is more suitable for us because the number of diffusion gradients we used ranges from 6-31.
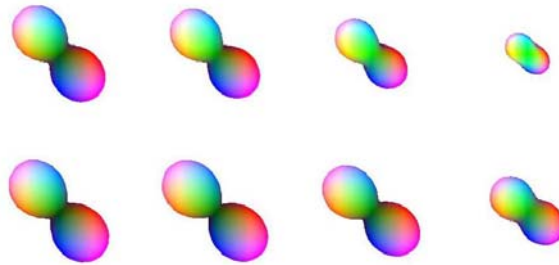
Figure 3. Parameterized surface representation of diffusion tensors. Diffusion surfaces show diffusivity as a function of direction. In this example, the tensors are oriented such that their principal direction is rotated about -45° from horizontal, and slightly through-plane. The orientation of the tensors is effectively conveyed using color (red-R/L, green-A/P, blue-S/I).

Visualization of diffusion data, whether using diffusion ellipsoids, a parameterized surface, or an FA map, often includes color coding. The color encoding of

orientation information (22,23) provides 3D directional information. The most common color coding scheme uses red for the right/left (R/L) direction, green for anterior/posterior (A/P) , and blue for superior/inferior (S/I). Examples of this color scheme are shown in Figure 3.

Histology

In this study, the microscopic structural and chemical composition of brain tissue provided by histology is considered the gold standard, and is compared to diffusion parameters of DMRI. Three main procedures – fixation, sectioning, and visualization – are involved in histology, and each of these procedures is briefly described next.

Fixation

Once a tissue sample is obtained through surgery, autopsy, or biopsy, it begins to undergo autolysis and degeneration of the tissue starts almost immediately. The purpose of fixation is to preserve the structural and chemical composition of tissues by stopping this degenerative process. Use of formaldehyde as a fixative was first proposed by Blum *et al* (24), and 4% solution of formaldehyde is the most commonly used fixative to this day. It has been shown that formaldehyde cross-links macromolecules such as proteins, glycoproteins, nucleic acids, and polysaccharides. This cross-linking process polymerizes protein and makes it gelatinous (25). However, the molecular process of formaldehyde fixation is still unknown, and under investigation. Formaldehyde has very low molecular weight (30 amu) and penetrates into tissues rapidly. However, the fixation process after

its initial penetration is gradual and an incubation period of at least 24 hours at room temperature is recommended (26).

Tissue shrinkage is one of the biggest sources of concern in quantitative histology. Previous experiments showed that the shrinkage during fixation itself is minimal (27,28) and the most severe tissue distortions, such as shrinkage and tearing, occur due to aggressive sectioning, staining, and mounting procedures following fixation (28).

Sectioning

Tissues are sectioned in thin slices that range from a few to a few hundred micrometers for microscopic examination, using a microtome. In this study, a freezing microtome is used to cut frozen brain tissues manually for light microscopy analysis.

Visualization

Sectioned tissues are stained to increase the contrast of desired structures, increasing the quality of visualization. In this study, our tissue sections were stained for myelin, which wraps around axons to provide insulation and facilitate the transmission of nerve impulses along the axons. The observation of stained myelin sheaths in histological sections provides valuable structural and directional information on fiber bundles. Many of the commonly used staining techniques for normal and degenerative myelin are listed in Bencroft *et al* (29), such as the Weigert-Pal method, Loyez method, and Luxol fast blue method. Gallyas' silver staining (30) is a popular method for visualizing myelin that is use in this study. Once the desired contrast is achieved through staining, the tissue

sections are available for analysis using light microscopy at high spatial resolution. In this study, the myelin stained fibers were photographed at high spatial resolution for direct comparisons with DTI data.

Image Registration

In the field of medical imaging, the comparison of data between multiple subjects, comparison of data from different imaging modalities from the same subject, and combinations of both, are often required. Comparison of multiple datasets is facilitated by bringing them together in a common data space. For example, positron emission tomography (PET) and CT are sensitive to two very different physical properties of the sample. The information provided by PET and CT are valuable by themselves, but in some studies, viewing both data together can provide more valuable insight. However, image properties such as resolution, field of view, and contrast may differ between the datasets and simply lining them up side by side is often not sufficient for accurate comparison or overlay. One solution is to transform the PET image data to the CT image space in order to align corresponding structures more accurately. In this case the PET image being transformed to the CT image space would be referred to as a target image and the CT image would be referred to as a reference image. The process of applying one or more transformations to a target image to align it with a reference is called registration.

Linear and nonlinear transformations are two major classes of transformation. Linear registration includes four simple operations - translation, rotation, scaling and shearing, the operations which preserve vector addition and scalar multiplication relations.

Rigid registration involves only rotation and translation operations. Affine registration includes all four operations of translation, rotation, scaling, and shearing. Note that rigid registration is just a special case of affine registration. Nonrigid registration involves operations which do not preserve vector addition and scalar multiplication, and have no simple matrix representation.

The process of registration often involves many iterative loops of transformation. At the end of each loop, the resulting image is compared with a reference image to check the quality of alignment. This process is repeated until a maximum (or minimum) of a similarity measure using optimization algorithms, such as Powell's method (31), is found. The two main similarity measures used during the process are featured-based and intensity-based registration.

Feature-based registration uses image landmarks to assess the quality of image alignment. The landmarks can be manually chosen anatomical landmarks, external markers attached to a subject before imaging, or the entire surface of a structure. The transformations are then applied to the landmarks. Once the registration algorithm finds a transformation that minimizes the sum of the squared distances between each pair of corresponding landmarks, the whole image is transformed.

The intensity-based method is similar to the feature-based registration method, but it does not use image landmarks. Instead, the iterative algorithm is applied to a chosen patch of a target image. The target image patch is compared to the corresponding patch of the reference using a similarity measure of the patch intensity values. Transformation parameters are updated until the similarity measure reaches its maximum (or minimum, depending on the characteristics of the measure). The whole image set is

then transformed accordingly. Unlike in the feature-based algorithm where the sum of the squared distances is used as the similarity measure, statistics measuring the similarity of the intensities are used in the intensity-based registration method. Correlation coefficient (CC) and mutual information (MI) are used most frequently (32). Mutual information was initially introduced in Information Theory (33) and is especially popular because unlike CC, MI does not assume a linear relationship between voxel intensities of the reference and target image, enabling intermodality image registration.

Related Studies

Registration of Histological Data

During registration between histological and MRI images, linear registration is first utilized to address 3D global tissue deformations of histological volumes. Such deformations are caused by histological processing procedures such as tissue fixation, embedding, as well as other mechanical effects. Examples of such tissue deformations include global volume shrinkage and shearing. These 3D global tissue deformations are most easily corrected when the 3D data are registered to another undistorted 3D data set of the same sample. Because construction of a spatially consistent and continuous 3D volume from histological data can be challenging due to large nonlinear tissue distortions, an undistorted 3D volume is often constructed from digital images taken during tissue sectioning. Serial photographs of the tissue block are called a blockface data set (34). It has been shown in previous studies that the acquisition of the intermediate blockface data aids the overall registration to produce more robust registration results (35,36). This is due to the fact that the blockface volume contains minimal distortions and can serves as a

reference point for the next, more complicated registration step between the magnetic resonance imaging (MRI) and histological data. The method was adapted as early as 1988 to correlate histological sections with MR images to analyze nerve roots (37) and, more recently, Toga *et al* have extended the method to the processing of a whole human head and brain cryosectioning to create a spatially consistent brain atlas (35). Several studies have utilized this method to improve registration between histological and MRI data (36,38,39).

One of the challenges in registering MRI to histological data is the tissue distortion that is introduced into histological sections during the tissue processing steps described in the previous section. These distortions are often local and require complicated and time consuming solutions. For this reason, many studies have either opted for a more qualitative data comparison without image registration (40,41) or utilized linear registration to correct only the global distortions (42,43). While these approaches may provide a more time efficient experimental design, they are insufficient for quantitative data analysis at high spatial resolution. These studies often require a combination of both linear and nonlinear registration.

Nonlinear registration, which involves operations which do not preserve vector addition and scalar multiplication, is an appropriate method for correcting distortions that are more local. Before nonlinear registration is performed, linear registration is often used as a preliminary step to provide a good initialization to the nonlinear algorithm. In many cases, linear registration alone provides sufficient initialization, but for other cases, such as histological images that contain severe artifacts, it is necessary to preprocess the target image before applying the linear transformation. In order to obtain good registration

between MRI and histological data, one has to address major sources of deformation that are specific to histological data, such as tissue tearing and relative movement of different hemispheres or other smaller parts of the brain. Breen *et al* developed an interactive method for correcting spatial distortions in histology and utilized the method to register histology samples to corresponding MR images (44). During their distortion correction process, significant tearing was corrected using a thin plate spline (TPS) warping method. Pitiot *et al* developed a piecewise affine registration method and took a more automated approach in addressing the issue of movement of gyri and other smaller parts of the brain better (45). More recently, Dauguet *et al* was able to successfully reconstruct a 3D histological volume and register the volume to the corresponding MRI volume by incorporating a hemi-rigid transformation. This approach was taken to specifically address the problem of movement of different hemispheres of a brain observed in histological data (38).

Validation of DMRI

DMRI is a relatively new and developing field and there are a number of questions that still need to be answered about the information it provides. These questions include whether fiber bundles can be discriminated in the presence of intravoxel fiber crossing and partial volume averaging, as well as more fundamental questions such as how different structures contribute to apparent diffusion parameters. In recognition of the need for further investigation, many groups have studied DMRI using different approaches, such as simulation, phantom, as well as animal experiments. For simulation studies, Lu et al (46) developed a Bayesian tensor regularization method and validated

this with simulated data, Peled et al (47) proposed a two-tensor model and validated this method with a simulated data, and Chen et al (48) has developed a simulated curvature phantom to validate a streamline fiber tracking algorithm. For phantom studies, studies, Lin (49) and Perrin (50) used phantoms to validate their improved DMRI methods, while Watanabe (51) and Pullens (52) have focused more on developing gold standard phantoms for DMRI.

Simulation & phantom studies offer advantages because experiments can be tightly controlled, and one can perform more accurate quantitative data analysis since the true values are known. For animal studies, however, the true values are often unknown and difficult to measure, and investigators have turned to other gold standard measurements for validation of DMRI data. Although animal studies are conducted in a less tightly controlled environment with many more variables to consider, they provide more realistic tests of DMRI.

Lin *et al* (53) used manganese enhanced T1-weighted MR images as the gold standard in their effort to validate DTI tractography methods. The manganese-enhanced optic track was effectively visualized, providing a reference of the true fiber tract which was compared to DTI fibers, revealing good agreement. The acquisition of T1-weighted MR images is relatively easy, compared to that of histological data. However, T1-weighted MR images are not suitable for validation studies at a high level of spatial resolution. For this reason other validation studies used histological data as their gold standard instead.

D'Arceuil *et al* performed a comprehensive DMRI parameter optimization study in order to acquire high resolution DMRI images of *ex vivo* non-human primate brains

(54,55). In the study, the use of exogenous contrast agent (Gd-DTPA) as well as the effect of fixation on different diffusion parameters was investigated. The findings of this study helped to address many questions regarding *ex vivo* DMRI, demonstrating that *ex vivo* animal models can indeed be used to validate DMRI methods such as DTI, diffusion spectrum imaging (DSI), diffusion tractography, and q-space imaging (QSI).

The study by Kaufman *et al* (6) is one of the earliest DTI validation studies that compared the coherence of myelin stained fibers with FA. The analysis of a region in the anterior cingulum bundle showed that DTI provides important information about white matter morphology on a microscopic scale. In the study by Schmahmann *et al* (56), the long association pathways observed by DSI were validated with histological observations of the fibers made using the autoradiographic technique (57,58). The study demonstrated that DSI can resolve crossing fibers with better precision than DTI and that imaging of the complex long association pathways is feasible.

Another diffusion tractography validation study was done by Dauguet *et* al (59), where a quantitative validation of 3D DTI fiber tracts of a macaque was performed by comparing the data with the three dimensional histological fiber tract. The histological fiber tract was traced by injecting a neural tract tracer (WGA-HRP) in the motor and somatosensory region and the three dimensional histological fiber tract was reconstructed from the digital two dimensional (2D) micrographs of the histological sections. General agreement between the DTI and histological fiber tracts was noted. A quantitative validation of fiber orientation distribution (FOD) measurements was performed by Leergaard *et al* (60) using QSI of a rat brain. The study showed that accurate FOD

estimates can be obtained in regions with complex microarchitecture with an intrinsic orientation error of approximately five to six degrees.

Some studies have also been carried out to validate DTI by comparing the data with histological data of a pathologic condition. In the study done by Schmierer *et al* (61), the feasibility of using diffusion parameters as a predictor for the degree of disability in multiple sclerosis was investigated by correlating mean diffusivity (MD) and FA with histological indices of myelin content. It was shown that FA and MD are affected by myelin content and axonal content. Other studies have found correlations between DMRI data and histology of cardiac (62-64) and skeletal muscle (65).

CHAPTER III

ACCURACY OF IMAGE REGISTRATION BETWEEN MRI AND LIGHT
MICROSCOPY IN THE EX-VIVO OWL MONKEY BRAIN

Introduction

Macroscopic anatomical structures and functional relationships of the central nervous system (CNS) have been extensively studied using non-invasive methods such as magnetic resonance imaging (MRI), computer tomography (CT), and positron emission tomography (PET). Recently, diffusion tensor imaging (DTI) has become another important tool in studying CNS structure and connectivity. On a microscopic scale, histological analysis provides information about the brain's cytoarchitecture. Combining data across these modalities and distance scales provides new information: a better understanding of contrast mechanisms in the non-invasive images and the ability to infer microscopic tissue properties across the entire brain, in vivo.

The goal of this study was to develop a registration procedure that can successfully align MRI data with histological data within the histological image space. This would allow a direct comparison between MRI data and gold-standard information about the microscopic structural and chemical composition of brain tissue provided by histology. The result would be better characterized tools for understanding the CNS.

Histology

Simply defined as the study of tissue, histology involves three main processes–fixation, sectioning, and visualization. Once a tissue sample is obtained through surgery,

autopsy, or biopsy, it begins to undergo autolysis and the degenerative process starts almost immediately. The purpose of fixation is to preserve the structural and chemical composition of tissues by stopping this degenerative process. Use of formaldehyde as a fixative was first proposed by Blum (24), and 4% solution of formaldehyde is the most commonly used choice of fixative to this day. Formaldehyde has very low molecular weight (30 amu) and penetrates into tissues rapidly. However, the fixation process after its initial penetration is gradual and an incubation period of at least 24 hours at room temperature is recommended (26).

Tissue shrinkage is one of the biggest sources of concern during histology. Previous experiments have showed that the shrinkage during fixation itself is minimal (27,28), but the most severe forms of tissue distortions such as shrinkage, tearing, and folding, occur due to aggressive sectioning, staining, and mounting procedures following fixation (28). Tissues are sectioned in thin slices that range from a few to a few hundred micrometers for microscopic examination, using a microtome. In this study, a freezing microtome is used to cut frozen brain tissues manually for light microscopy analysis.

Sectioned tissues are stained to increase the contrast of desired structures, increasing the quality of visualization. In this study, tissue sections are stained for myelin, which wraps around axons to provide insulation and facilitate the transmission of nerve impulses along the axons. The observation of stained myelin sheaths in histological sections provides valuable structural and directional information on fiber bundles. Many of the commonly used staining techniques for normal and degenerative myelin are listed in Bencroft *et al* (29), such as the Weigert-Pal method, Loyez method, and Luxol fast blue method. Gallyas silver staining (30) is another popular method for staining myelin

that is used in this study. Once the desired contrast is achieved through staining, the tissue sections are available for analysis using light microscopy at high spatial resolution.

Registration

In the field of medical imaging, the comparison of data between histological and MRI data is often required. The information provided by MRI is valuable by itself, but investigating it in conjunction with histological data can provide insight into the sources of contrast in the MRI images. However, image properties such as resolution, field of view, and contrast will likely be very different between the datasets and simply overlaying the data is usually insufficient for accurate alignment and comparison. Reliable comparison of multiple datasets requires transforming them to a common data space--the process of applying one or more transformations to an image to align it with a reference image is called registration. Two major classes of registration are linear and nonlinear registration.

Linear registration includes four simple operations - translation, rotation, scaling and shearing, which preserve vector addition and scalar multiplication relations. Rigid registration refers to a registration process that involves only rotation and translation operations while affine registration includes all four operations of translation, rotation, scaling, and shearing.

During the registration between histological and MRI images, we used linear registration first to address three dimensional (3D) global tissue deformations of the histological volumes. Volume shrinkage and shearing are caused by tissue fixation and embedding, as well as other mechanical effects. It has been shown in previous studies

that photographs of the tissue block acquired during sectioning ('blockface" images) can be used to produce more robust registration results (35). These images, assembled into a 3D volume dataset, provide a relatively undistorted intermediate reference space between the MRI and the histological data. Several studies have utilized this method to improve registration between histological volume and MRI data (36,38,39).

In addition to the global distortions described above, other tissue distortions are local and require complicated and often time consuming corrections. For this reason, many studies have either opted for a more qualitative data comparison without image registration (40,41) or utilized linear registration to correct for only the global distortions (42,43). While these approaches may be time efficient, they are insufficient for studies that require more quantitative data analysis. In that case, a combination of both linear and nonlinear registration is usually required.

Nonlinear registration involves operations that do not preserve vector addition and scalar multiplication. For this reason, it is an appropriate method for correcting distortions that are more local. Before nonlinear registration is performed, linear registration is often used as a preliminary step to provide good initialization for the nonlinear algorithm. In many cases, linear registration provides sufficient initialization. However, in order to obtain good registration between MRI and histological data, one often has to address sources of deformations that are specific to histological data, such as tissue tearing and movement of separated tissue segments on the slide (e.g., different hemispheres or other smaller parts of the brain). Breen *et al* developed an interactive method for correcting spatial distortions in histology and used the method to register histology samples to corresponding MR images (44). During their distortion correction

procedure, significant tearing in the tissue section was corrected using a thin plate spline (TPS) warping method. Pitiot *et al* developed a piecewise affine registration method and took a more automated approach in addressing the issue of movement of gyri and other smaller parts of a brain (45). More recently, Dauguet *et al* were able to successfully reconstruct a 3D histological volume and register it to the corresponding MRI volume by incorporating a hemi-rigid transformation. This approach was taken specifically to address the problem of movement of different hemispheres of the brain observed in histological sections (38).

Method

Image Acquisition

i. *Magnetic Resonance Imaging*

All animal procedures were approved by the Vanderbilt Animal Care and Use Committee. A male owl monkey was given a lethal dose of barbiturate and perfused through the heart with buffered physiological saline. Fixation was performed by perfusing with 4% paraformaldehyde in phosphate buffer, then by 4% paraformaldehyde in phosphate buffer with 10% sucrose. The fixed brain was removed from the skull and kept in 30% sucrose for approximately 24 hours. The brain was then transferred into a phosphate buffered saline (PBS) medium and scanned on a Varian 9.4 Tesla, 21 cm bore magnet using a multi-slice, pulse gradient spin echo sequence (b = 0 and 1309 s/mm^2 , 21 diffusion weighting directions, TE = 31.2 ms, TR = 17.1 s, 128 x 128 x 132 image

volume matrix, 0.3 mm isotropic voxel resolution). After the image acquisition, one iteration of the anisotropic smoothing algorithm proposed by Ding *et al* (17) was performed to improve signal to noise ratio (SNR). Parameters used were $\rho = 2SD$ and C = 3, where SD is the standard deviation of noise and C is a threshold parameter used to control the degree of smoothing. Non-diffusion weighted (T2-w) images were assembled into a 3D volume dataset, and the brain image was extracted from background for registration purposes (66).

ii. Blockface

Twenty four hours after the MR imaging, the brain was embedded in dry ice and sectioned on a microtome at 50 micron thickness in the coronal plane, where the position of the brain stayed constant during cutting and only the blade of the microtome moved. Using a Cannon EOS20D digital camera with 70-300 mm zoom lens, the tissue block was digitally photographed prior to cutting every third section, resulting in a through-plane resolution of 150 microns. The initial in-plane resolution of the original blockface images was 16 μm isotropic. The original high resolution blockface images were downsampled to 256 x 256 with 0.15 mm isotropic voxel resolution for more efficient data processing.

Because the position of the brain stayed constant during sectioning, the 3D blockface volume could be constructed by simply stacking the two dimensional (2D) images of each section. The reconstructed volume was then corrected for the section-to-section intensity variation which was caused by the inconsistent light reflection from the frozen tissue block surface during photograph acquisition. This section-to-section

intensity variation was corrected by adjusting the intensity of cortical gray matter of each section to be within a similar intensity range of the gray scale blockface images. The final blockface volume dataset was acquired by manually segmenting the brain from its dry ice background. Although time consuming, the manual segmentation of the brain was necessary because the contrast between the brain and dry ice was low and automatic segmentation methods failed to segment the edges of the brain successfully.

iii. Light micrograph

Sectioning of the brain block was followed by histochemical processing, where tissue sections were stained for myelin using Gallyas' silver method (30). Staining was performed on floating tissue sections, which were then mounted on glass slides manually for further investigation under a light microscope. A Nikon DXM1200F digital camera mounted on a Nikon E-800 microscope was used to take images of the stained sections at 0.5x magnification. The brain was segmented from the background before further data analysis. An example of a blockface image and the corresponding light micrograph (before brain segmentation) is shown in Figure 4.

(a)   (b)
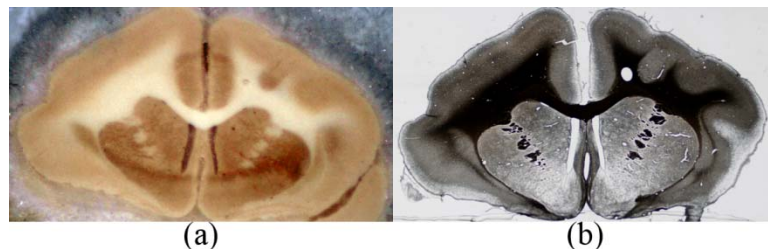
Figure 4. Blockface and histological images. (a) An example of a blockface image before the brain is segmented from its dry ice background (b) An example of a light micrograph image before the brain is segmented from its background. The section is the same as shown in (a), and is stained for myelin using the Gallyas silverstaining method.

Image Registration

        A multi-step registration scheme was developed in order to transfer MRI image data to the histological image space. First, volume datasets of the DTI and blockface images were constructed. Dimensions of the T2-wimage volume matrix were 128 x 128 x 132 with 0.3 mm isotropic voxel resolution. The original high resolution blockface and light micrograph volume dataset were down sampled to 256 x 256 x 222 with 0.15 mm isotropic voxel resolution for ease of data processing. The T2-w volume was then registered to the blockface volume using a combination of linear (i.e., rigid and anisotropic scaling) (32,67) and nonlinear registration with the Adaptive Bases Algorithm (ABA) (68). Next, a section of interest was chosen and the corresponding blockface and light micrograph images were registered in two dimensions using both linear and nonlinear registration with ABA. Figure 5 summarizes the steps of this procedure. A more detailed description of the multi-step registration scheme is presented below.
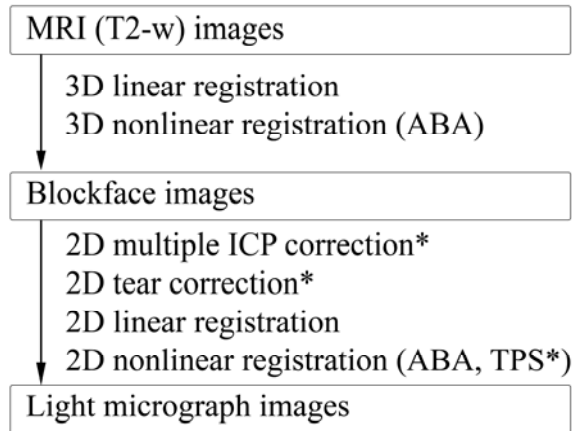
Figure 5. Multi-step registration workflow summary. Three major datasets – MRI, blockface, and light microscopy datasets – were acquired. The datasets were registered to each other using a combination of linear and nonlinear registration. For selected histological sections with tissue tearing or relative displacement of different parts of brain, 2D rigid tear correction and/or 2D multiple ICP correction was performed as a preprocessing step. In some cases, an additional step using TPS was necessary after nonlinear registration of the blockface images.

i. *T2-w → Blockface*

Linear registration was performed using a mutual information (MI) based method similar to that of Maes (32). Partial volume (PV) interpolation was used for intensity interpolation of the transformed reference image (32). Powell's multidimensional direction set method was used to maximize the MI registration criterion, using Brent's optimization algorithm for line minimization (31). Powell's criterion was set to 10^{-5}, Brent's to 10^{-3}, and the maximum number of iterations was set to 600. The number of bins for joint histogram calculation was set to 64 x 64 and three resolution levels were used. Transformation in the *MRI to blockface* step was performed by optimizing first the in-plane parameters, then the through-plane parameters.

In addition to the linear transformations, nonlinear registration was performed using ABA (68). Fifteen control point levels and two resolution levels were used to

28

determine the transformation scale and spatial resolution. Sixty four bins were used for joint histogram calculation and a Jacobian threshold of 0.05 was used as an optimization constraint. Optimization of a basis function was halted when the cost function's improvement was below 0.0005.

ii.   *Blockface → Light micrograph*

Due to the extensive artifacts in some micrographs (see Figure 6), additional preprocessing was necessary for the affected sections to ensure robust registration results. The preprocessing procedure was developed to address two major types of artifacts: tissue tearing and relative displacement of different pieces of tissue on the slide.
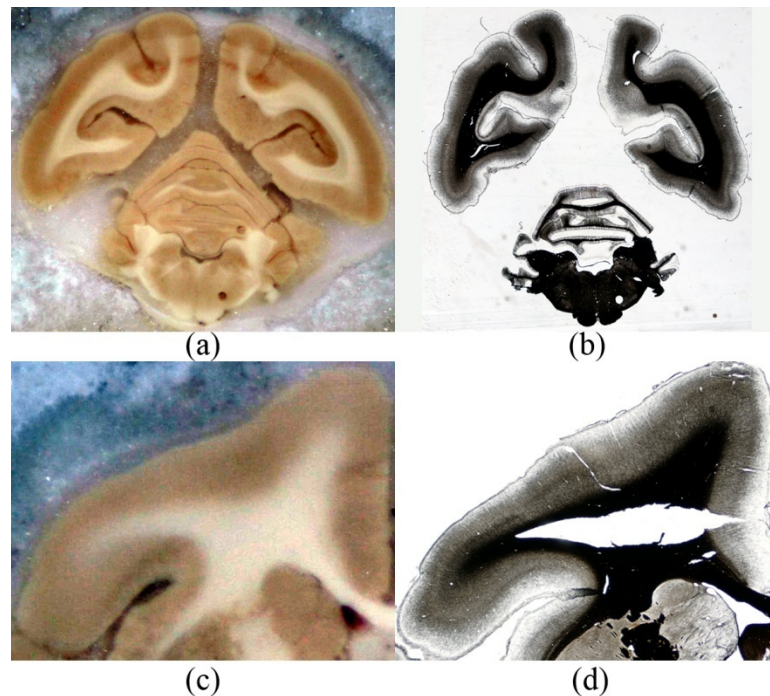
Figure 6. Image artifacts introduced during histological processing. (a), (c) Undistorted blockface images. (b) Example of relative displacement of the hemispheres and the cerebellum. (d) Example of tissue tearing.

- *Correction for severe tissue tearing artifacts*

Figure 6 (a) and (d) shows light micrographs of myelin stained tissue sections with severe tearing of tissue. In order to correct a large tearing artifact, the contour of the torn region was first selected by a user. Examples of the outlines are shown in Figure 7 (b) and (e). Because of the procedure used to manipulate the tissue sections, tissue tears were nearly horizontal (anatomical right-left direction) in the coronal sections. According to the location of the tear, the user can choose to fix the tear using one of three options: i) translate the image data *below* the tear upward to meet the top edge of the tear, 2) translate the image data *above* the tear downward to meet the lower edge of the tear, or3) translate image data both above and below the tear to meet the center line of the torn region. If the user chooses the third scheme, the center line is computed automatically based on the contour of the torn region and the distance between each pixel on the contour and the centerline is also calculated. Pixels in image columns passing through the tear are translated towards the center line, according to the calculated distances. Figure 7 (c) shows the image after translating the tissue up while Figure 7 (f) shows the image after moving the tissues toward the center line. Generally, the option that minimized the mean pixel displacement was chosen.
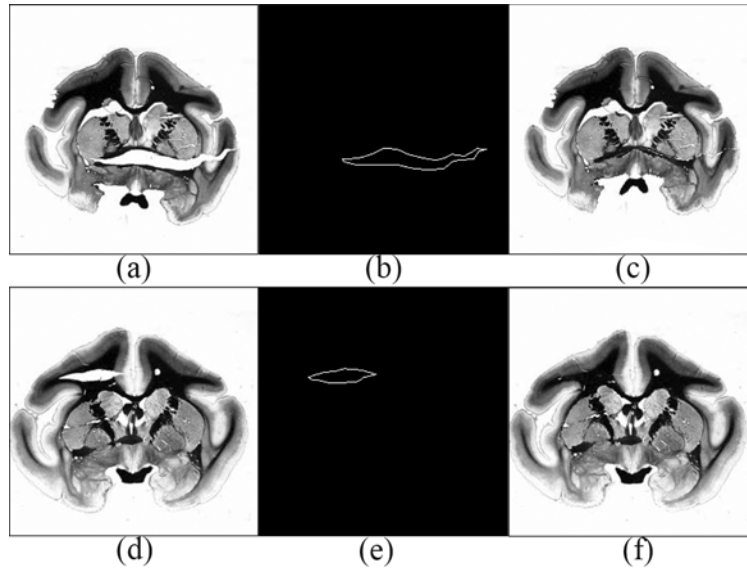
Figure 7. Contour selection for 2D tear correction. (a), (d) Original light micrographs with severe tissue tearing artifacts. (b), (e) User selected contours of tissue tear edges. (c), (f) Result of tear correction method.

- *Correction for relative displacement of different pieces of tissue*

Each of the myelin stained sections was mounted on a glass slide manually. In some sections, different pieces of the tissue, such as left and right hemispheres, are not physically connected and so must be mounted and oriented on a slide separately. Figure 6 (b) shows an example of a stained section in which the two hemispheres and the cerebellum have all moved away from each other. This relative displacement of different parts of the tissue section is more obvious when compared to the corresponding undistorted blockface section, as shown in Figure 6 (a).

Once the sections that need to be corrected for excessive relative displacements were identified, regions of interest (ROIs) containing the same piece of tissue in the blockface image and micrograph were selected manually.

The iterative closest point (ICP) algorithm (69) was then applied to the selected ROIs.

The ICP algorithm is a technique that has been applied widely to surface-based registration in medical images. It calculates the transformation and distance between two point sets extracted from two surfaces iteratively. Once the distance is found to converge to a user-selected threshold, the algorithm is terminated. In this study, we applied the ICP algorithm to multiple tissue components. For each pair of corresponding ROIs, suppose $X = \{x_i, i = 1, 2, ...N\}$ is a point set in the micrograph and Y the point set in the blockface image. The algorithm then proceeds as follows (also refer to (70) for more information):

1. $\forall x_i \in X$, find the closest point y_i in the surface (?)Y;

2. Compute the rotation R and translation t through optimizing the mean square disparity function D:

$$D = \sqrt{(1/N)\sum_{i}^{N}\|Rx_i + t - y_i\|^2} \; ; \tag{1}$$

3. Apply the R and t to the point set X to obtain the new $X' = RX + t$;

4. Compute the new distance D' between X' and Y. If the absolute difference between D and D' is less than 1e-5 (selected empirically), terminate the procedure. Otherwise, let $X = X'$, and repeat the procedure from step 1.

The ICP algorithm was applied to each pair of ROIs to generate the corresponding rigid body transformations. The transformations are applied to the different tissue pieces to deform the micrograph data to the (undistorted) blockface image space.

Following the preprocessing steps described above, a combination of 2D linear and nonlinear registration was performed on each of the corresponding block and light micrograph sections, using the same registration parameters as used during T2-w→ blockface registration. Two different deformation fields were generated after performing both registration steps. The first deformation field described the transformation of the 3D T2-w image volume into the 3D blockface image volume space, and the second deformation field described the transformation of a 2D blockface image into the 2D light micrograph image space. Each of the deformation fields was applied to the original T2-w volume data to generate a registered T2-w image that could be aligned with the corresponding light micrograph data in the histological data space.

Accuracy measurement

Alignment of structures after each registration step (T2-w → blockface, blockface → micrograph) was evaluated both qualitatively and quantitatively. Qualitative assessment was performed by superimposing the transformed target images (MRI data) onto reference images (light micrographs) for visual inspection. After the initial visual inspection, landmarks were manually selected throughout the MRI data volume. Corresponding landmarks in the blockface and light micrograph volumes were selected,

and the distance between corresponding landmarks in the registered target and reference volumes provided a measure of registration accuracy.

Results

T2-w → Blockface

Construction of the blockface volume involved stacking the original 2D images without image registration because each of the blockface photographs was acquired from a stationary brain sample, cut with a moving blade. For this reason, the alignment of the T2-w and blockface volume datasets was good in many regions after only linear registration. The result of the 3D registration of the MRI (more specifically, T2-w) volume to blockface volume was qualitatively assessed by aligning the volumes in the original blockface volume data space, as shown in Figure 8. Column (a) of Figure 8 shows orthogonal views of the T2-w volume (displayed in blue for better contrast with the blockface images).Column (b) shows the same T2-w data overlaid on the original blockface volume. Column (c) shows the T2-w volume after it was linearly registered to the blockface volume, overlaid on the original blockface volume. Notice the significant decrease of misalignment when compared to the superimposed images of column (b). Any remaining misalignment of structures after linear registration, such as in some cortical and cerebellar areas, was addressed through nonlinear registration using ABA. Column (d) shows the T2-w volume after both linear and nonlinear registration to the blockface volume, overlaid on the blockface volume. Good overall alignment of structures was observed after registration.

(a)   (b)   (c)   (d)   (e)
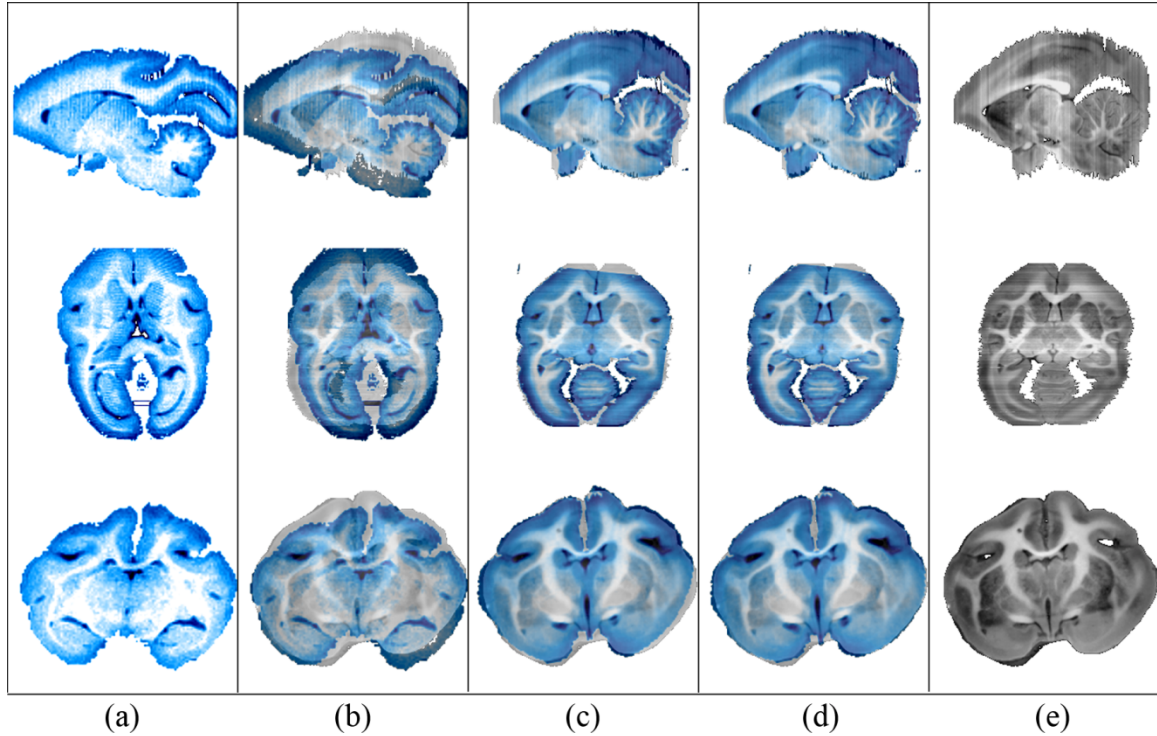
Figure 8. 3D registration of MRI (T2-w) to blockface volumes. (a) Orthogonal views of the original non-diffusion weighted (T2-w) image volume. (b) Original T2-w images superimposed on blockface images, (c) T2-w images after linear registration, and (d) T2-w images after linear and nonlinear registration are overlaid on original blockface images, reproduced in (e).

Blockface → Light micrograph

Visual inspection of each of the myelin stained sections was performed in order to identify those with severe tissue tearing and/or relative displacement of separated pieces of the tissue. Once identified, those sections were preprocessed using tear correction and multiple ICP methods to prepare the sections better for the linear and nonlinear registration steps to follow. Comparison of results between affected sections that had not and those that had been preprocessed demonstrated that the preprocessing step provided more robust registration, as shown in Figure 9 and Figure 10.
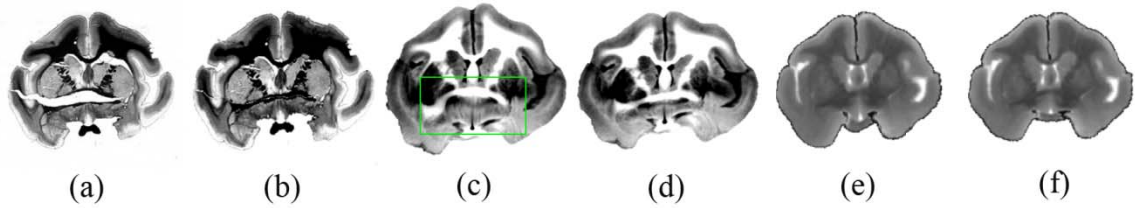
Figure 9. Example of application of the tear correction method. (a) An original light micrograph, (b) the micrograph after closing the tear, (c) & (d) the corresponding blockface image deformed to match (a) and (b), respectively. (e) & (f) MR images registered to (a) & (b), respectively. Note the green region in (c) was locally stretched by the nonlinear registration algorithm in order to match the hole in (a), causing a distortion.
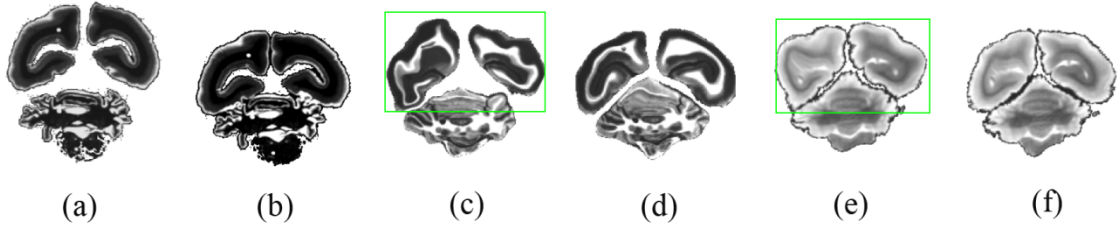
Figure 10. Example of application of the multiple component ICP method. (a) The original light micrograph of mounted tissue, (b) the corrected micrograph using the ICP algorithm, (c) & (d) the deformed blockface images and (e) & (f) MR images registered to (a) & (b), respectively. The green region shows the large distortion when the ICP algorithm was not applied to the light micrograph.

Figure 9 demonstrates an example of tear correction performed on a myelin stained section and its effect on image registration. Figure 9 (a) shows a section with severe tissue tearing artifacts caused by a vertical tensile force along the anterior commissure as well as another tear between the corpus callosum and internal capsule. Figure 9 (b) shows the result of tear correction on the torn section. Figure 9 (c) and (e) show the result of overall registration (linear and nonlinear registration) of the blockface and MR images, respectively, when they were registered to the myelin stained section

that was not preprocessed. Figure 9 (d) and (f) show the result of the overall registration of the blockface and MR images, respectively, when they were registered to the myelin stained section that was preprocessed. The results shown in Figure 9 (d) and (f) demonstrate that the tear correction produces more accurate registration (compare to (b)).

Figure 10 demonstrates an example of the multiple ICP algorithm applied to a myelin stained section and its effect on the image registration. Figure 10 (a) shows a myelin stained section where three pieces of brain tissue were displaced from their original locations during the mounting procedure. Figure 10 (c) and (e) show the blockface image and T2-w image, respectively, registered to the myelin stained section that was not preprocessed. It can be seen that the registration algorithm is not able to account for large displacements of structures and produces an incorrectly deformed result. Figure 10 (d) and (f), on the other hand, show the blockface image and T2-w image, respectively, when they were registered to the myelin stained section that was preprocessed using the multiple ICP algorithm. The improvement compared to the results shown in Figure 10 (c) and (e) is evident. Hence, the multiple ICP algorithm provides a better initialization for the overall registration process, leading to a more accurate result. It should be noted that although cerebellar sections that had moved during mounting were also preprocessed, the smaller size and complex structure of the cerebellum sometimes resulted in tearing and movement, as well as missing pieces of the tissue that rendered it almost impossible to register with its corresponding blockface sections, even after the preprocessing step. For this reason, and because it was not the focus of this study, the cerebellum was excluded from any further analysis.

An example of the 2D registration of a blockface section and the corresponding light micrograph is shown in Figure 11. The top row of Figure 11 allows for visual inspection of the registration over the whole section. Figure 11 (a) and (e) are the images of the original blockface and myelin stained section. Figure 11 (b), (c) and (d) show the original blockface section, the blockface section after linear registration, and after linear and nonlinear registration, respectively, superimposed on the myelin stained section. It can be seen that linear registration improves the alignment of the sections substantially, and some remaining tissue artifacts around the cortical area are corrected with further, nonlinear registration. The bottom row of Figure 11 shows the registration result in a more local region around the left external capsule, highlighted within the green box shown in Figure 11 (j). Figure 11 (f) shows the original blockface section with the outline of the myelin stained section's white matter (WM) overlaid in red. Figure 11 (g), (h) and (i) provide a zoomed-in view of the change in the external capsule after each registration step. Notice how, in Figure 11 (i), the outlines of the external capsule of blockface and myelin stained sections are aligned well.
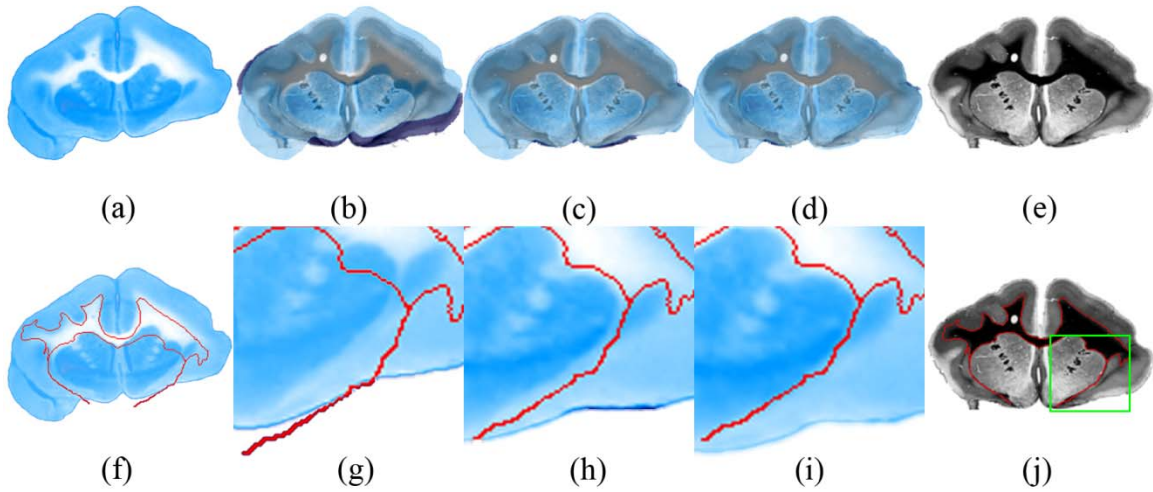
Figure 11. 2D registration of a blockface section to a corresponding myelin stained section. (a) Original blockface section. (b) Original blockface section, (c) blockface section after linear registration, and (d) blockface section after linear and nonlinear registration overlaid on the myelin stained section, respectively. (e) Original myelin stained section. (f) Original blockface section. The red line represents the white matter (WM) outline of the corresponding myelin stained section, also outlined in (j). (g) A region of interest (ROI), outlined in green in (j), is selected from the original blockface section. (h) ROI in the blockface section after linear registration. (i) ROI in the blockface section after linear and nonlinear registration. In (g-i), the WM outline (in red) of the corresponding myelin stained section is also overlaid for comparison.

T2-w → Blockface → Light micrograph

A total of 291 landmarks were selected over the whole brain volume within the original T2-w volume. Corresponding points were then identified manually in the blockface and light micrograph volumes. The corresponding points provided the 'true' locations of the landmarks within their respective image spaces. The landmarks selected in the T2-w dataset were then transferred into the blockface and micrograph image spaces to provide a measure of error for different stages of the overall registration process (i.e., T2-w → blockface linear, T2-w → blockface linear and nonlinear, blockface → light micrograph linear, blockface→ light micrograph linear and nonlinear, and T2-w → light

micrograph linear and nonlinear). The measure of registration error for each stage was the distance between the corresponding points transformed to the same image space. In Figure 12, the distribution of the landmarks used is visualized within the surface rendered image of the original MRI volume. Each of the landmarks is color coded according to the corresponding error measurement, which is summarized in Table 1.
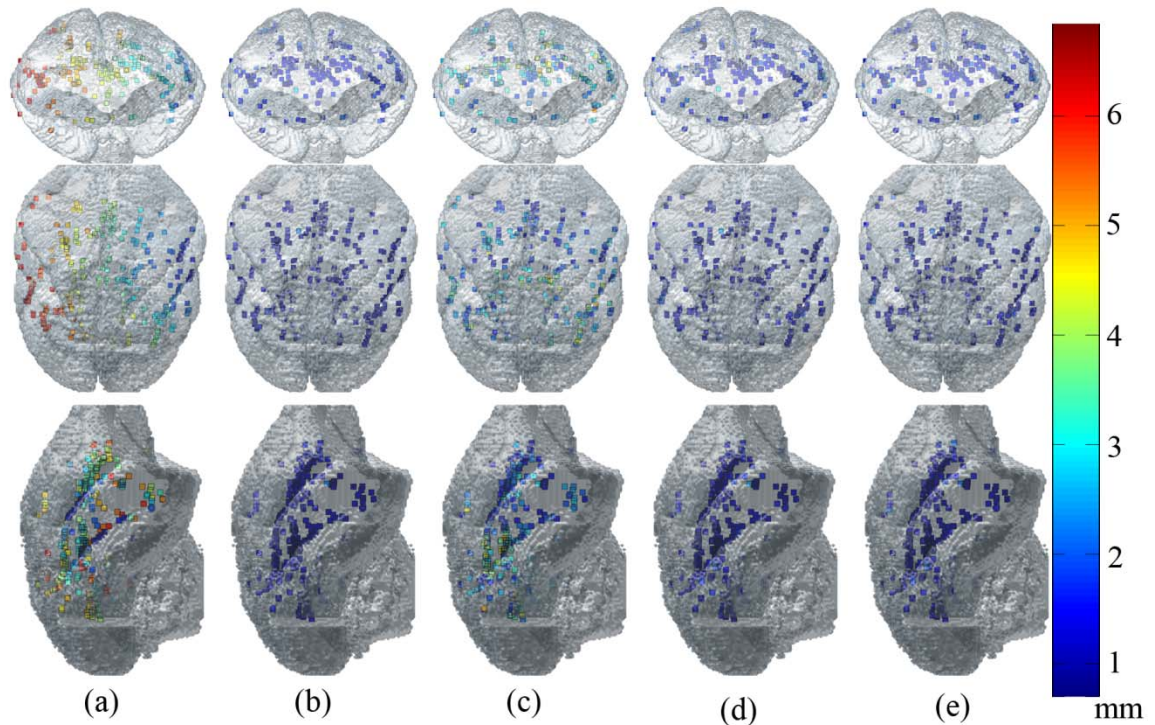
Figure 12. Distribution of landmarks used for registration accuracy measurements. Chosen landmarks are visualized within the surface rendered image of the original MRI volume. Each of the landmarks is colorcoded according to the registration error between landmarks in (a) original MRI image space and original blockface image space, (b) registered (linear & nonlinear) MRI image space and original blockface image space, (c) original blockface image space and original light micrograph space, (d) registered (linear & nonlinear) blockface image space and original light micrograph space, (e) registered (linear & nonlinear) MRI image space and original light micrograph space. The size of the voxels is 0.3 mm^3.

Table 1. Registration accuracy as measured by the distance between corresponding landmarks chosen from T2-w, blockface, and light micrograph volume data.

	T2-w → blockface	T2-w (in Blockface image space) → light micrograph	T2-w → light micrograph
Initial error (mm)	3.84 ± 1.39	1.87 ± 1.07	4.55 ± 1.80
After linear registration (mm)	0.326 ± 0.18* (t-stat: 44.02, p < 0.01)	1.08 ± 1.16* (t-stat: 11.62, p < 0.01)	n/a
After linear and nonlinear registration (mm)	0.261 ± 0.18* (t-stat: 8.46, p < 0.01)	0.319 ± 0.28* (t-stat: 11.25, p < 0.01)	0.324 ± 0.78* (t-stat: 30.40, p < 0.01)

* Statistically significant ($p < 0.05$) reduction in error relative to the previous step.

The original T2-w volume was resized from 128 x 128 x 132 to 256 x 256 x 222 through interpolation only for the purpose of calculating the initial error between the MR volume and blockface and light micrograph volumes before registration. Note that the initial error measurements include rotation as well, resulting in large error measurements. The measured initial error between MR and blockface volumes was 3.84 ± 1.39 mm. Error between the blockface data and the T2-w data that was linearly registered was 0.326 ± 0.18 mm, which is slightly over the size of the original MR voxel (0.3 mm). This confirmed the previous visual observation that the T2-w → blockface registration was good, even after performing only a linear transformation. Error between the blockface and T2-w data that was linearly and nonlinearly registered to the blockface was 0.261 ± 0.18 mm, which shows improvement over simple linear registration (0.326 ±

0.18 mm). It should also be noted that the error after both linear and nonlinear registration is less than the size of the MR voxel.

The large initial error (1.87 $\pm$ 1.07 mm, ~ 6 MR voxels) between the light micrograph points and the T2-w data in the blockface space is due to large tissue distortions that were introduced during histological processing and mounting. Even after linear registration, the error is relatively high at 1.08 $\pm$ 1.16 mm. Combination of the preprocessing step, linear and nonlinear registration improves the error between the micrograph points and the T2-w data registered to the micrograph to 0.319 $\pm$ 0.28 mm. Finally, the overall registration accuracy measurement between T2-w data and light micrograph data was measured using the landmarks selected in the original T2-w data space and light micrograph space. The initial error was 4.55 $\pm$ 1.80 mm and the overall error was 0.324 $\pm$ 0.78 mm. Note that the large initial error measurement results from including rotation error between the two data sets. The change in error after each of the registration steps was statistically significant ($p < 0.05$).

Discussion

In this study, a registration workflow that transfers MR data into histological image space was developed and its accuracy was measured. The acquisition of blockface data was essential because it provided an undistorted three dimensional image of the brain before sectioning and served as an intermediate step in registering MR data to distorted light micrographs. The post processing of the image data proved to be very time consuming, however, due to the lack of an automated means to segment the brain from

the surrounding dry ice. Other studies have encountered similar problems (38) and reported progress using new dyes for dry ice.

One of the biggest challenges for the study was the severe tissue distortion that was introduced into light micrographs during histological processing and mounting. This distortion was difficult to control because the whole process – sectioning, staining, and mounting - was performed manually. There are several possible solutions to this problem, for example the use of an automated cryomicrotome stage and acetate tape transfer system that would allow one to preserve the histological structures. Other studies have used this method successfully and also reported improved registration results due to decreased tissue distortions (71,72). The use of acetate film tape, however, leaves a residue on sectioned tissues and may not be ideal for studies that require staining of floating sections. Another possible solution is to use a celloidin medium that would stay with the sectioned tissues throughout the staining and mounting procedure (73,74).

Despite these limitations, we were able to successfully register MRI data to the distorted light micrographs by preprocessing to correct severe local distortions then applying linear and nonlinear registration steps. The use of robust nonlinear registration (using ABA), in particular, was critical because it provided spatially adaptive and topologically consistent deformation fields (68). The procedure has allowed us to register light micrograph sections with mean error less than the size of an MR voxel.

The result of our study suggests that through the use of a carefully designed registration scheme, it is possible to register MR to histological data, even in the presence of severe tissue distortions, such as tearing and displacement of different pieces of tissue.

This procedure can be useful for those who would like to study and compare histological microstructures with other imaging methods such as MRI.

Conclusion

Despite the rapid growth of different neuroimaging modalities, histological analysis of CNS still provides the gold standard for information about the brain's cytoarchitecture. Quantitative comparison of neuroimaging and histological data is facilitated by effective tools for cross-modality registration. In this study, a multi-step registration procedure is presented that enables an effective overlay of MRI and histological data in the histological image space. A blockface volume was reconstructed to provide an intermediate step for the overall registration process, which allowed for a more robust registration result. Two major types of tissue distortions– tissue tearing and movement of separated pieces of tissue- were corrected using a preprocessing procedure that implemented 2D tearing correction and the 2D multiple ICP algorithm. The accuracy of the overall (linear and nonlinear) registration workflow was assessed by measuring the discrepancy between the position of landmarks chosen in the MR image space, then transformed to the micrograph space, and the position of the corresponding points chosen in the micrograph space. In this study, it was shown that the registration procedure provides an effective means to quantitatively compare MRI and histological data with the average error comparable to the size of the original MR voxel (0.3mm).

CHAPTER IV

VALIDATION OF DIFFUSION MRI IN THE CENTRAL NERVOUS
SYSTEM USING LIGHT MICROSCOPY

Introduction

Diffusion tensor imaging (DTI) is rapidly becoming a mainstay of neuroimaging

studies. It has been used to characterize white matter lesions in individuals (75-79) and to

quantify group differences on a voxel-by-voxel basis across the entire brain (80-82). DTI

is also commonly used to reconstruct fiber pathways in the white matter (83-86). These

applications are based on the assumptions that diffusion anisotropy reflects white matter

microstructure and that the principal eigenvector of the tensor approximates the

orientation of fibers in a voxel. These measurements are at times complicated by factors

such as partial volume averaging of non-parallel fibers (87) and image noise and artifacts

(88,89), which limit the accuracy of diffusion tensor estimates. When DTI fiber tracking

produces erroneous pathways, the failure is usually ascribed to these causes, and more

robust tracking algorithms continue to be developed.

A number of studies have attempted to validate DTI and quantify the limitations

to its accuracy under various experimental conditions. Numerical simulations of the

effects of noise (88,89) and partial volume averaging (87) are in general agreement with

theoretical calculations (90,91) and similarly, numerical tests of fiber tracking algorithms

have quantified pathway errors for a range of conditions (84,92). Several studies have

also shown good agreement between diffusion MRI (dMRI) orientation estimates and

ground truth in phantom studies (49,50,93). These simulation and phantom studies have

provided important insights into the performance of DTI through analysis of specific and well characterized factors and their effects on DTI accuracy. More recently, several experimental studies involving comparisons of *ex vivo* diffusion data and corresponding tissue structure have been conducted. These provide a more comprehensive understanding of dMRI by comparing diffusion anisotropy with white matter properties such as fiber orientation distribution and fiber spread (6,60). Diffusion fiber tractography results have also been compared to known fiber pathways traced in *ex vivo* brain using an injected neural tract tracer, and showed good agreement (94).

The definition of a gold standard for fiber properties on a microscopic scale is an important component of a DTI validation experiment. While high resolution micrographs of stained tissue sections provide such a gold standard, manual data analysis is very labor intensive. In this study, DTI data and high resolution histological micrographs were acquired from an *ex vivo* owl monkey brain. The high resolution micrographs were analyzed using a Fourier domain filtering method to measure fiber properties efficiently. The measurements from each dataset were then quantitatively compared for validation purposes.

Methods

Image Acquisition

All animal procedures were approved by the Vanderbilt Animal Care and Use Committee. A male owl monkey was given a lethal dose of barbiturate and perfused through the heart with buffered physiological saline. Fixation was performed by

perfusing again with 4% paraformaldehyde in phosphate buffer, then by 4% paraformaldehyde in phosphate buffer with 10% sucrose. The fixed brain was removed from the skull and kept in 30% sucrose for approximately 24 hours. The brain was then transferred into a phosphate buffered saline (PBS) medium and scanned on a Varian 9.4 Tesla, 21 cm bore magnet using a multi-slice, pulse gradient spin echo sequence (b = 0 and 1309 s/mm^2, 21 diffusion weighting directions, TE = 31.2 ms, TR = 17.1 s, 128 x 128 x 132 image volume matrix, 0.3 mm isotropic voxel resolution, total scan time = 13 hrs). After image acquisition, one iteration of the anisotropic smoothing algorithm proposed by Ding *et al* (17) was performed to improve signal to noise ratio (SNR). Parameters used were $\rho = 2SD$ and C = 3, where SD is the standard deviation of noise and C is a threshold parameter used to control the degree of smoothing. Non-diffusion weighted (T2-w) images were also obtained and assembled into a three dimensional (3D) volume dataset for registration purposes.

Twenty four hours after imaging, the brain was embedded in dry ice and sectioned on a microtome at 50 micron thickness in the coronal plane. Using a Cannon EOS20D digital camera with 70-300 mm zoom lens, the tissue block was digitally photographed prior to cutting every third section, resulting in a through-plane resolution of 150 microns. The initial in-plane resolution of the blockface images was 16 μm isotropic. The tissue sections were then stained for myelin using Gallyas' silver method (30) and mounted on glass slides for light microscopy image acquisition. A Nikon DXM1200F digital camera mounted on a Nikon E-800 microscope was used to take images of the stained sections at 0.5x, 1x, 2x, 4x, 10x, and 20x magnification, as shown in Figure 13.
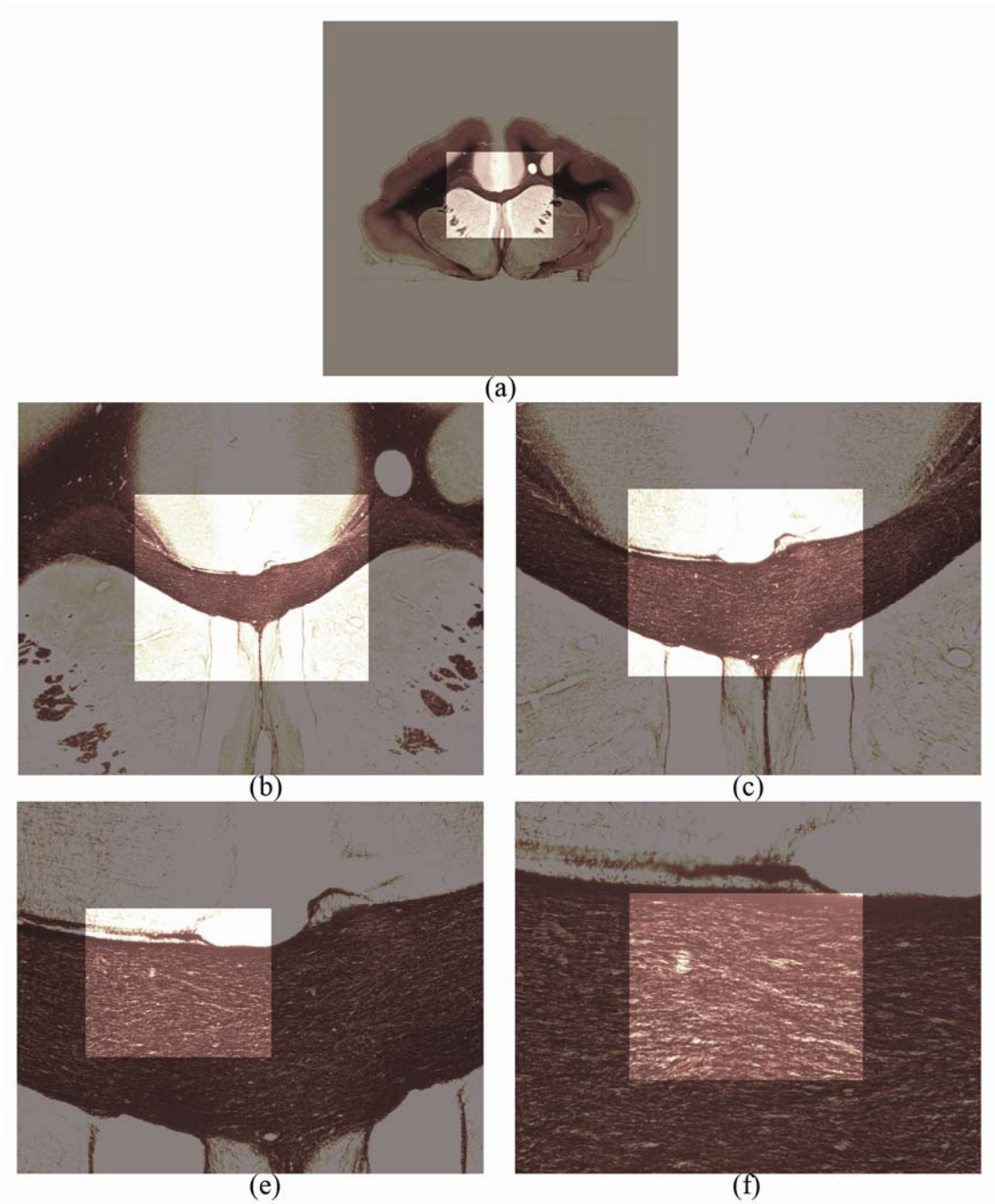
Figure 13. Iterative scheme for localizing a high resolution (20x) micrograph in a low resolution (0.5x) micrograph. At each step, the location of the field of view (FOV) of the higher magnification micrograph within the lower magnification image was obtained using 2D registration. (a) Scaled FOV of the 1x image is superimposed on the corresponding 0.5x image, (b) 2x FOV in 1x, (c) 4x FOV in 2x, (d) 10x FOV in 4x, and (e) 20x FOV in 10x.

Image Registration

In order to transfer the tensors in the original magnetic resonance (MR) image space to the high resolution light microscopy image space, a multi-step registration scheme was used. Figure 14 summarizes the steps of this procedure. First, the volume datasets of the DTI and blockface images were constructed. Dimensions of the DTI dataset were 128 x 128 x 132 with 0.3 mm isotropic voxel resolution, and those of the blockface volume dataset were downsampled to 256 x 256 x 222 with 0.15 x 0.15 x 0.15 mm voxel resolution. The T2-w dataset was then registered to the blockface dataset using a combination of linear (i.e., rigid and anisotropic scaling) (67) and nonlinear registration with the Adaptive Bases Algorithm (ABA) (68). Next, a section of interest was chosen and the corresponding blockface and low magnification (0.5x) micrograph were registered in 2D, again using both linear and nonlinear registration with ABA.
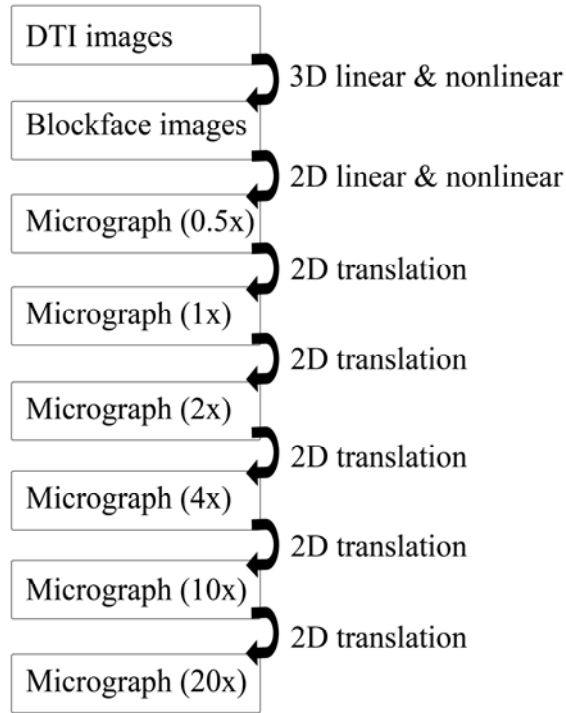
Figure 14. Registration scheme summary. Three major datasets – DTI, blockface, and light microscopy datasets – were obtained. Light microscopy data were obtained under multiple magnifications, ranging from the lowest of x0.5 to the highest of x20 magnification. Locations of the higher magnification images within lower magnification images were found using 2D registration (translations only), and the three major datasets were tied together using a combination of linear and nonlinear registration.

For both sets of registrations (T2-w → blockface, blockface → micrograph), linear registration was performed using a mutual information (MI) based method similar to that of Maes *et al* (32). Partial volume (PV) interpolation was used for intensity interpolation of the transformed reference image (32). Powell's multidimensional direction set method was used to maximize the statistical dependence, using Brent's one-dimensional optimization algorithm for line minimization (31). Powell's criterion was set to 10^{-5}, Brent's to 10^{-3}, and the maximum number of iterations was set to 600. The number of bins for joint histogram calculation was set to 64 x 64 and 3 resolution levels

were used. Transformation in the MRI to blockface step was performed by optimizing first the in-plane parameters, then the through-plane parameters. A set of in-plane transformations (two dimensional translations only) using MI as a similarity measure was performed in order to find the field of view of the high resolution micrographs within lower magnification micrographs of the same section, an example of which is shown in Figure 13.

In addition to the linear transformations, nonlinear registration was performed using ABA for both steps (T2-w → blockface, blockface → micrograph). Fifteen control point levels and two resolution levels were used to determine the transformation scale and spatial resolution. Sixty four bins were used for joint histogram calculation and a Jacobian threshold of 0.05 was used as an optimization constraint. Optimization of a basis function was halted when the cost function's improvement was below 0.0005.

Fiber Property Measurements

i. *Diffusion Imaging*

Diffusion tensors were calculated using the method of Basser *et al* (12). For each position in the target (micrograph) image space, the corresponding tensor in the DTI dataset was calculated using PV interpolation of the original diffusion weighted images. In order to preserve the orientation of the tensors relative to the tissue after registration, the tensors were rotated using the preservation of principal direction (PPD) reorientation strategy proposed by Alexander *et al* (95).

Fiber information in the light micrographs is inherently two dimensional, i.e., the orientation, coherence, and density of through-plane fibers cannot be measured using the simple Fourier domain filtering method. In order to ensure that micrograph measurements of fiber properties reflect all fibers in that volume of tissue, only those voxels containing mostly in-plane fibers are selected for detailed data analysis. This was done by selecting voxels in which diffusion was predominantly in-plane. In-plane diffusion was determined by the following criteria: either the first two eigenvectors (corresponding to the largest two eigenvalues of the tensor) were nearly in the plane of the micrograph or, if the second and third eigenvalues were nearly equal and much less than the first, and the principal eigenvector was nearly in the plane of the micrograph. (In all cases, 'nearly' implied a maximum deviation of 25°). The rationale for considering the second eigenvector is that crossing fibers should lie in the plane of the first two eigenvectors (at least in the simplest model). On the other hand, if all fibers are nearly parallel and diffusion has axial symmetry around the principal eigenvector, then the orientation of the second eigenvector is arbitrary (in the plane of symmetry), so the second eigenvector should be ignored in this case. Out of the initial dataset, 102 voxels with mostly in-plane fibers were selected for further data analysis.

The registered tensors were diagonalized in the plane of the micrograph. The principal in-plane eigenvector provided the DTI estimate of fiber orientation, projected onto the plane. In order to quantify the effect of fiber spread on diffusion anisotropy, the two dimensional fractional anisotropy (2D FA, i.e., the FA calculated using the two in-plane eigenvalues) was found for voxels with predominantly in-plane diffusion.

ii. Light Microscopy

The angular distribution of myelinated fibers was measured using Fourier domain (k-space) filtering (96) of high resolution micrographs (10x). This method is based on the fact that the 2D Fourier transform of a line in image space is non-zero on a line through the origin in k-space (at an orientation orthogonal to the image space line). In our implementation, the spatial frequency spectrum of a 300μm by 300μm patch of high resolution micrograph was filtered using 36 functions that pass spatial frequency components in a narrow range of angles. Each function was symmetric around the origin, forming opposing 'fan blades,' 10 degrees in width and weighted as follows:

$$H(f_r, \theta) = \frac{(1 - \beta f_r)}{\left\{ \left[1 + \left(\frac{f_L}{f_r} \right)^{2p} \right] \left[1 + \left(\frac{f_r}{f_H} \right)^{2q} \right] \right\}^{1/2}} \cos^\alpha \left(\frac{\theta - \theta_0}{B} \pi \right) \qquad (11)$$

where β is the slope of the weighting function, f_r is the normalized radial frequency, p is the order of the high pass filter, q is the order of the low pass filter, f_H is the upper cutoff frequency, f_L is the lower cutoff frequency, θ is the angle of the Fourier transform sample, θ_0 is the central angle of the desired fan blade, B is the angular bandwidth, and α is a weighting factor. For our design, β = 0.7, p = 6, q = 4, f_H = 0.5, f_L = 0.02, and α = 0.5. An example of the composite directional filter with θ = 137.5° and B = 10° is illustrated in Figure 15.
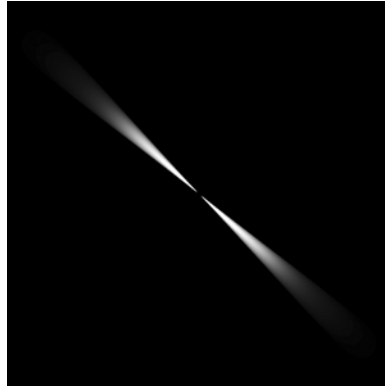
Figure 15. Composite directional filter in the Fourier domain. Each filter was designed using a combination of a fan filter, a Butterworth bandpass filter, a ramp-shaped lowpass filter, and a raised cosine window. $\theta = 137.5°$ and $B = 10°$

Each filter passed spatial frequencies near the center of the blade, attenuating them more as they approach the blade edges at the center angle +/- five degrees. The 36 filter functions differed only by rotation - the center-to-center separation of neighboring blades was five degrees (blades overlapped to provide more uniform sensitivity as a function of orientation).

The Fourier domain filters produced 36 filtered images containing fiber component information at corresponding orientations. Polar plots ('rose' plots) were used to visualize fiber orientation histograms which effectively display the dominant orientation and coherence of stained in-plane fibers. In the rose plot, the amplitude of the histogram at a particular orientation corresponds to the fraction of fibers at that angle. The peaks of the distribution (the petals) indicate the orientations of fiber bundles while the widths correspond to the degree of fiber coherence.

A simple measure of fiber density could be taken from the fiber to non-fiber area ratio, calculated by thresholding light micrograph images. However, this method would not be able to discriminate between linear structures (fibers) and features with other

shapes (e.g., vessels and micrograph artifacts). Similarly, a simple intensity threshold would not account for crossing fibers in the density measurement. Ideally, the density measurement reflects the volume fraction of fibers in the 3D volume of the tissue section, and therefore should count the area of both fibers at a crossing point. In order to address these concerns, a different measure of fiber density using the Fourier domain filtering method was utilized. A summed image for a patch of micrograph was created by thresholding and summing the 36 filtered fiber images described above. Note that this involves adding the binary filtered images, so regions of intersecting fibers are counted multiple times. Since crossing regions are counted multiple times, the density measured in this way can be greater than one. This results from the fact that all fibers in the tissue volume are projected onto the 2D plane of the micrograph and contribute to filtered area measurements in the image. The performance of the fiber spread and density measurement using Fourier domain filtering was tested using simulated fiber micrographs, an example of which is shown in Figure 16. A total of 100 simulated patches with varying degree of angular distribution width, fiber density, and peak orientation were analyzed using the Fourier domain filtering method. For each of the patches, the true fiber angle standard deviation and the measured fiber angle standard deviation data were compared. In addition, the true fiber density and measured fiber density were obtained and compared.
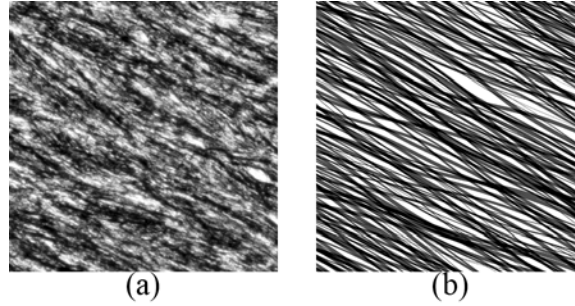
Figure 16. Actual and simulated micrograph patches. (a) A high resolution micrograph of fibers in the corpus callosum, imaged at x20 magnification. Measured fiber orientation is 153 degrees to the horizontal axis. (b) Simulated high resolution micrograph of fibers. Fiber orientation was chosen from random numbers with a normal distribution ($\mu = 153°$, $\sigma = 24°$).

Results

Tensor Transformation

The location of the high resolution micrograph within a low resolution (0.5x) micrograph was used to place tensors at the appropriate positions in the high resolution micrographs. Overall alignment of the tensors with the myelin stained fibers was very good. The agreement within fiber bundles with strong directionality, such as in corpus callosum, was excellent, as shown in Figure 17 (a) and (b). Note that each tensor is rendered as a surface for which the distance between the origin and the surface in each direction is proportional to the water diffusivity in that direction:

$$\vec{r}(\theta,\phi) = (D(\theta,\phi)\sin(\theta)\cos(\phi), D(\theta,\phi)\sin(\theta)\sin(\phi), D(\theta,\phi)\cos(\theta)) \qquad (12)$$

where θ is the polar angle and ϕ is the azimuthal angle.

Figure 17 (c) shows a region with complex fiber structure and the corresponding tensors. It can be seen from Figure 17 (c) that diffusion tensors are more isotropic and provide less orientation information where fibers cross. This also implies that tensors are limited by MRI spatial resolution and are unable to reflect the fine details of fiber pathways less than one voxel in diameter.
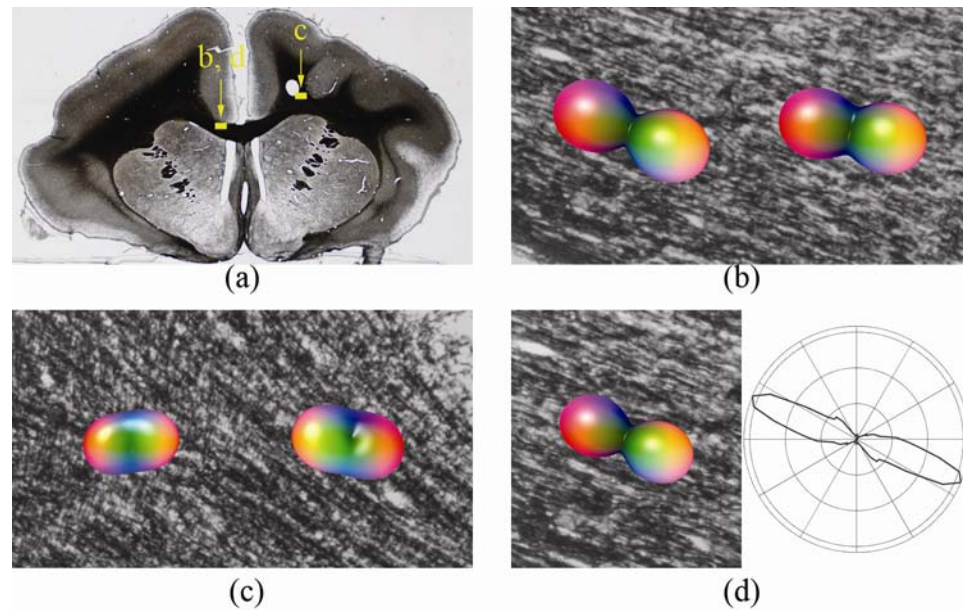
Figure 17. Tensors overlaid on light microscopy images. The registered tensors are overlaid on the corresponding high magnification micrographs. Relative locations of the high magnification (20x) micrographs (b) and (c) are outlined in the lower magnification (0.5x) micrograph (a). All diffusion surfaces are scaled by (in-plane) fractional anisotropy. The surfaces therefore tend to be small and spherical where anisotropy is low. Fiber orientation of myelin stained fibers on the left in (b) is visualized using a rose plot (d).

Fiber Property Measurements

The performance of the Fourier domain filtering method, used to measure the angular distribution of myelinated fibers, was tested using Monte Carlo simulation. The relationship between the measured fiber spread (i.e., standard deviation) of the simulated

micrograph and the true fiber spread is shown in Figure 18 (a). The measured angular spread is very nearly equal to the true value ($y = 0.987 * x + 0.009$, $R^2 = 0.998$, where y is the measured value and x is the true value). The relationship between the measured and true fiber density, shown in Figure 18 (b), is also nearly linear ($y = 1.002x - 0.022$, $R^2 = 0.988$). These comparisons strongly suggest that the Fourier domain filtering method is a reliable tool for measuring fiber properties of high resolution micrographs. The filtering method on real data is demonstrated in Figure 19, where tensor diffusion surfaces and rose plots are overlaid on high resolution micrographs for visual comparison. Figure 19 (a) and (b) are from a region with more coherent fibers while (c) and (d) are from a region with crossing groups of fibers. It can be seen that the Fourier domain filtering method is able to identify the orientations of crossing fiber groups effectively.
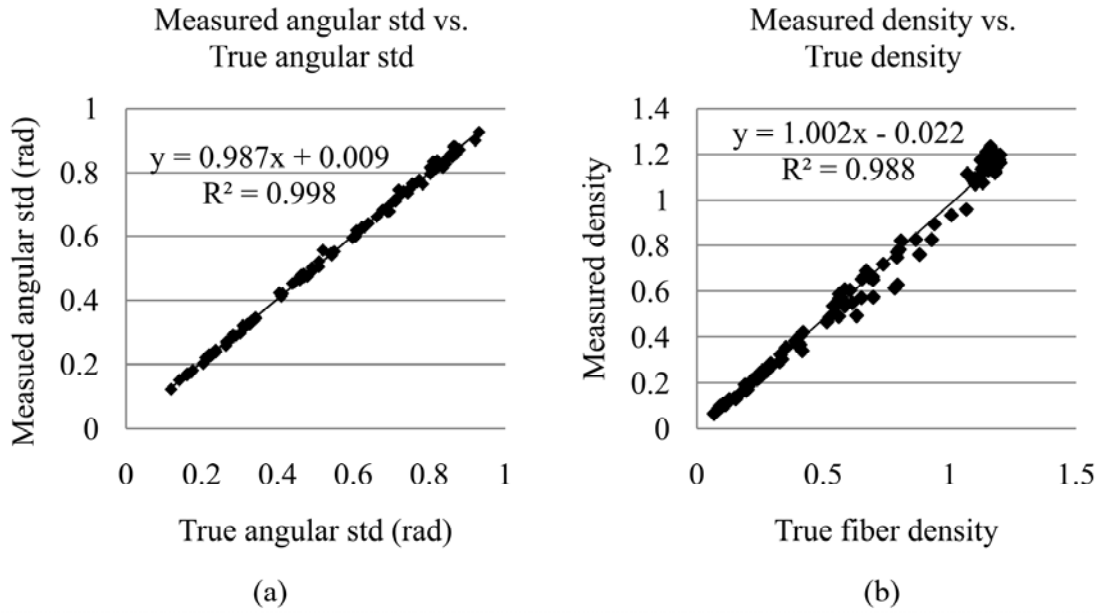
Figure 18. Performance of Fourier domain filtering method on simulated data. (a) Fiber angle standard deviation of simulated micrographs, calculated by the Fourier domain filtering method, is plotted against the true angle standard deviation. (b) Fiber density of simulated micrographs is plotted against the true fiber density. Both demonstrate a high correlation between the true and measured data.
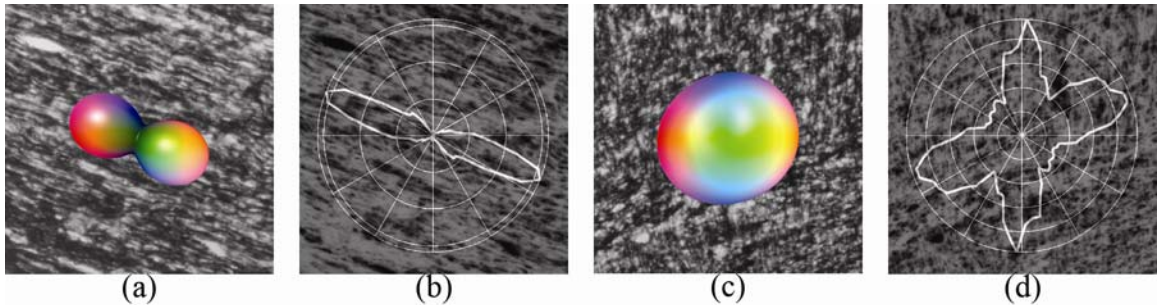
Figure 19. Examples of Fourier domain filtering method on micrographs. (a) A highly anisotropic diffusion surface is overlaid on the corresponding region of a high resolution micrograph. (b) The angular distribution of fibers in the same micrograph patch (shown in reversed contrast to make fibers bright) is visualized using a rose plot. (c) An isotropic diffusion surface is overlaid on the corresponding micrograph patch. (d) The angular distribution of crossing fibers in the same micrograph patch as in (c) is visualized using a rose plot.

For each in-plane tensor overlaid on the high resolution micrographs, a corresponding region of interest, a 'patch' with in-plane dimensions of the DTI pixels, was identified in the micrographs. Rose plots were used to visualize fiber orientation histograms that reveal the dominant orientation and coherence of stained fibers within each region. These were compared to the tensor registered with that region. An example of the analysis in the corpus callosum is shown in Figure 17 (d). The in-plane principal eigenvector of the tensor in Figure 17 (d) is at 157 degrees to the horizontal axis, and the dominant fiber orientation in the micrograph is at 153 +/- 12 degrees. Figure 20 shows a histogram of the measured angle differences between the true fiber orientation (from high resolution micrographs) and the fiber orientation from diffusion imaging of all the patches. The peak of the histogram indicates that on average, tensors differ from their true fiber orientation by less than 10 degrees (about the limit of accuracy of the Fourier filtering algorithm). As the tensors become isotropic, ambiguity in the fiber orientation measured by the first eigenvector increases and the measured angle differences may increase.
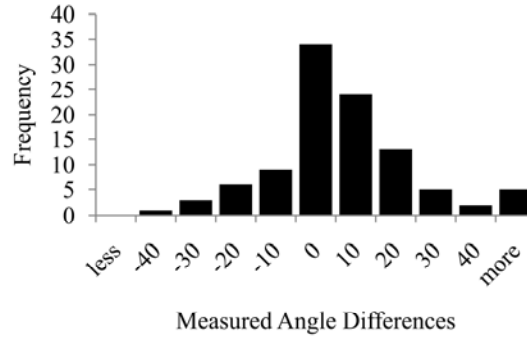
Figure 20. Histogram of the measured angle differences. The differences between the true fiber orientation measured in high resolution light micrographs and the fiber orientation estimated from diffusion imaging are plotted (in units of degrees).

Multivariate regression analysis was performed, with 2D FA as the dependent variable and fiber spread and density measurements as the independent variables, as shown in Table 2 (the overall F-statistic was 23.9, $p < 0.05$). Increases in fiber spread, measured as the standard deviation of fiber angles within the high resolution micrograph, are associated with decreases in FA ($p < 0.001$) and increases in fiber density are associated with increases in FA ($p < 0.05$). This relationship is described by the following model: FA = 0.997 - 1.032 * spread + 0.267 * density.   Note that this relationship should be expected to hold only within the range of the conditions tested in this experiment (i.e., fiber spread from 0.30 to 0.90 radians and density from 0.44 to 2.53). Nevertheless, within this range the model shows that FA has a stronger dependence on spread than on density (e.g., doubling spread produces a larger change in FA than does doubling fiber density). In Figure 21, several micrographs with similar density or spread are shown to illustrate the relationship between FA and fiber spread and density. Figure 21 (a) shows micrographs with similar degree of fiber spread (0.36 to 0.44 radian) but varying fiber density and their corresponding rose plots. Figure 21 (b) shows light micrographs of

similar fiber density (1.50 to 1.69) but varying degree of fiber spread and their

corresponding rose plots.

Table 2. Regression of FA (dependent variable) versus fiber spread and fiber density
(independent variables)

Variable	β	t-statistics	p-value
Constant	0.997	14.333	$6.87 \text{ x } e^{-26}$
Fiber Spread	-1.032	-5.898	$5.13 \text{ x } e^{-8}$
Fiber Density	0.267	2.163	0.0330

F-statistic: 23.9 (p = 0.0306)
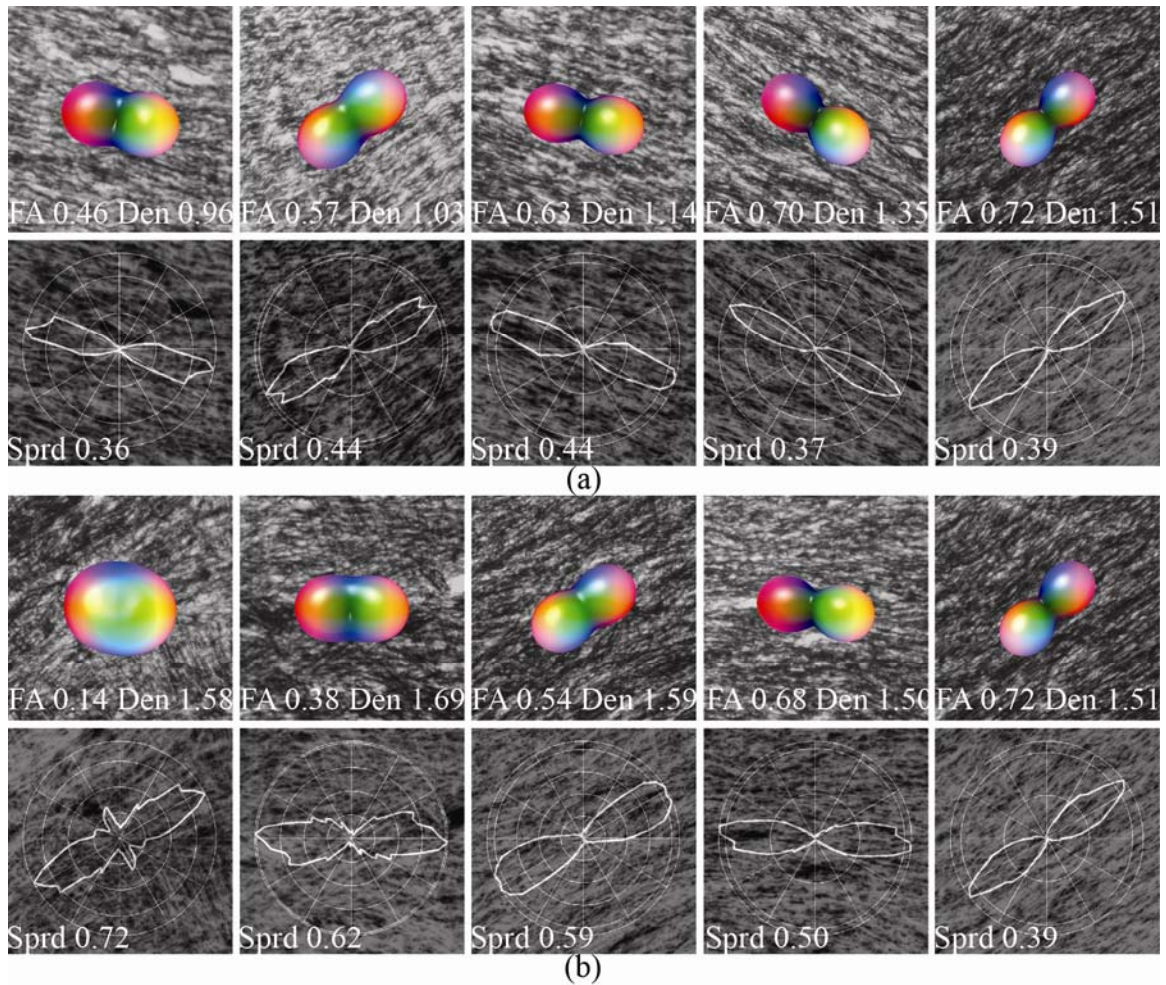
Figure 21. Example light micrographs demonstrating the relationship between FA, fiber spread, and fiber density (a) Micrographs with similar fiber spread (0.36 to 0.44 radian) but varying density are shown. As the fibers become denser, FA increases. (b) Micrographs with similar fiber density (1.50 to 1.69) but varying fiber spread are shown with the corresponding rose plots. As the fibers become more coherent, FA increases.

Discussion

Analysis of high resolution micrographs was performed using a Fourier domain filtering method which provided an effective means to automatically extract fiber property measurements. We have shown in this study that the agreement was good between tensors derived from DTI and myelin stained fibers analyzed via light

microscopy, and the degree of diffusion anisotropy was highly correlated with rose plot width.

Due to the high diffusion gradients and small voxel sizes required for high spatial resolution DTI, the data suffer from inherently low SNR. Possible solutions to this problem include increasing the number of signal averages and using an effective noise-reduction, post-processing procedure. In order to improve upon our SNR, we acquired DTI images for a long time (> 13 hrs) and used the anisotropic smoothing algorithm proposed by Ding *et al* (17). A single iteration of the algorithm was performed in order to avoid any excess smoothing and the consequent corruption of tensor orientation information.

Because the brain tissue block was sectioned, stained, and mounted manually, various mounting artifacts, such as tissue tearing, folding, and shearing, were inevitable. The use of nonlinear registration, especially the utilization of ABA, was essential in correcting for these mounting artifacts. The algorithm permitted spatially adaptive deformation field modeling and therefore was effective for most tissue sections. The algorithm imposes a constraint that prevented topologically incorrect registration. After registration, the fiber orientation measurements from DTI and light microscopy show a good correlation, as seen in Figure 20

It should be noted that the fiber spread and density information from high resolution micrographs is limited to two dimensions. In consideration of this limitation we only selected voxels with mostly in-plane principal eigenvectors for data analysis, and it was shown in Table 2 and Figure 21 that there exists good correlation between the FA and two dimensional fiber properties measured from histological data. However,

structures in the brain cannot generally be treated as two dimensional, and advancing our methods to obtain through-plane information from tissue sections would improve our ability to probe and compare information between DTI and histological data. In addition to being dimensionally limited, our histological data lack information on other cellular properties that probably affect FA, such as axon thickness, degree of myelination, and diffusivity in the various water compartments. Measurement of other such fiber properties would allow a more comprehensive understanding of DTI.

Conclusion

Since the initial realization of the ability of NMR to observe molecular diffusion (8), the field has grown extensively and has become a valuable tool, with applications in a wide range of diseases. Because DTI is the only imaging method to date that can probe white matter microstructure *in vivo*, the accuracy of the information provided by the method is all the more important. However, DTI is still developing and faces a number of unsolved problems, such as resolving crossing fibers and determining how different structures interact to produce observed DTI parameters. Having a methodology to directly compare fiber directionality and distribution measured from DTI and histological data will help to answer these questions. In this study, we developed such a methodology and demonstrated that an excellent correlation exists between the principal fiber directional measurements from DTI and myelin-stained histological sections. It was also shown that, although limited in spatial and angular resolution, DTI is able to identify regions with complex fiber structure with considerable accuracy.

CHAPTER V

CONCLUSION

Since the initial realization of the ability of NMR to observe molecular diffusion

(8), the field of DTI has grown extensively and DTI has become a valuable tool, with

applications in a wide range of diseases. Because DTI is the only imaging method to date

that can probe white matter microstructure *in vivo*, the accuracy of the information

provided by the method is all the more important. However, DTI is still developing and

faces a number of unsolved problems, such as resolving crossing fibers and determining

how different structures interact to produce observed DTI parameters. Having a

methodology to directly compare fiber directionality and distribution measured from DTI

and histological data will help to answer these questions. In this study, we developed such

a methodology and compared fiber properties measured by DTI and histology.

The development of a methodology to directly compare DTI and histological

data was important for this study, because despite the rapid growth of neuroimaging

methods, histological analysis of the CNS still provides the gold standard for information

about the brain's cytoarchitecture. A multi-step registration workflow of DTI data was

developed that provided an accurate overlay of DTI and histological data in the

histological image space. A blockface volume was reconstructed to provide an

intermediate step for the overall registration process, and the use of this spatially

consistent volume allowed for a more robust registration result. Two major tissue

distortions – tissue tearing and movement of different parts of the brain, introduced

during histological processing, were corrected using a preprocessing procedure that

utilized a 2D tearing correction method and the 2D multiple component ICP algorithm. The accuracy of the overall (linear and nonlinear) registration workflow was assessed by measuring the differences between the position of the registered landmarks chosen in the MR image space and the position of the same landmarks chosen in the histological image space. The presented registration workflow provided an effective means to quantitatively compare DTI and histological data with an average error less than 0.3 mm, which is the size of the original MR voxel.

Using the developed procedures, diffusion tensors were positioned in the reference (micrograph) image space and rotated using the PPD method (95) in order to preserve the orientation of the tensors relative to surrounding anatomy. For each of the corresponding voxels, the angular distribution of myelinated fibers was then measured using Fourier domain (k-space) filtering (96) of high resolution (10x) micrographs, which provided us with a measure of fiber coherence and fiber density. The performance of the Fourier domain filtering method was tested using Monte Carlo simulation and it was shown that it is a reliable tool for measuring fiber properties in high resolution micrographs. In order to ensure that micrograph measurements of fiber properties reflect all fibers in that volume of tissue, only those voxels containing mostly in-plane fibers were selected for detailed data analysis.

The overall alignment of the tensors with the myelin stained fibers was very good. The agreement within fiber bundles with strong directionality, such as in the corpus callosum, was excellent, and on average, tensors differed from their true fiber orientation by less than 10 degrees (about the limit of accuracy of the Fourier filtering algorithm). Multivariate regression analysis was performed, with 2D FA as the dependent variable

and fiber spread and density measurements as the independent variables. It was demonstrated that an excellent correlation exists between the fiber property measurements from DTI and myelin-stained histological sections. It was also shown that, although limited in spatial and angular resolution, DTI is able to identify regions with complex fiber structure with considerable accuracy.

APPENDIX A

LIST OF PROGRAMS USED

The purpose of this appendix is to provide more detailed description of the programs and their functions that were written for data construction, processing, and analysis related to this dissertation project. A flowchart has been created for easier visualization in Figure 22.
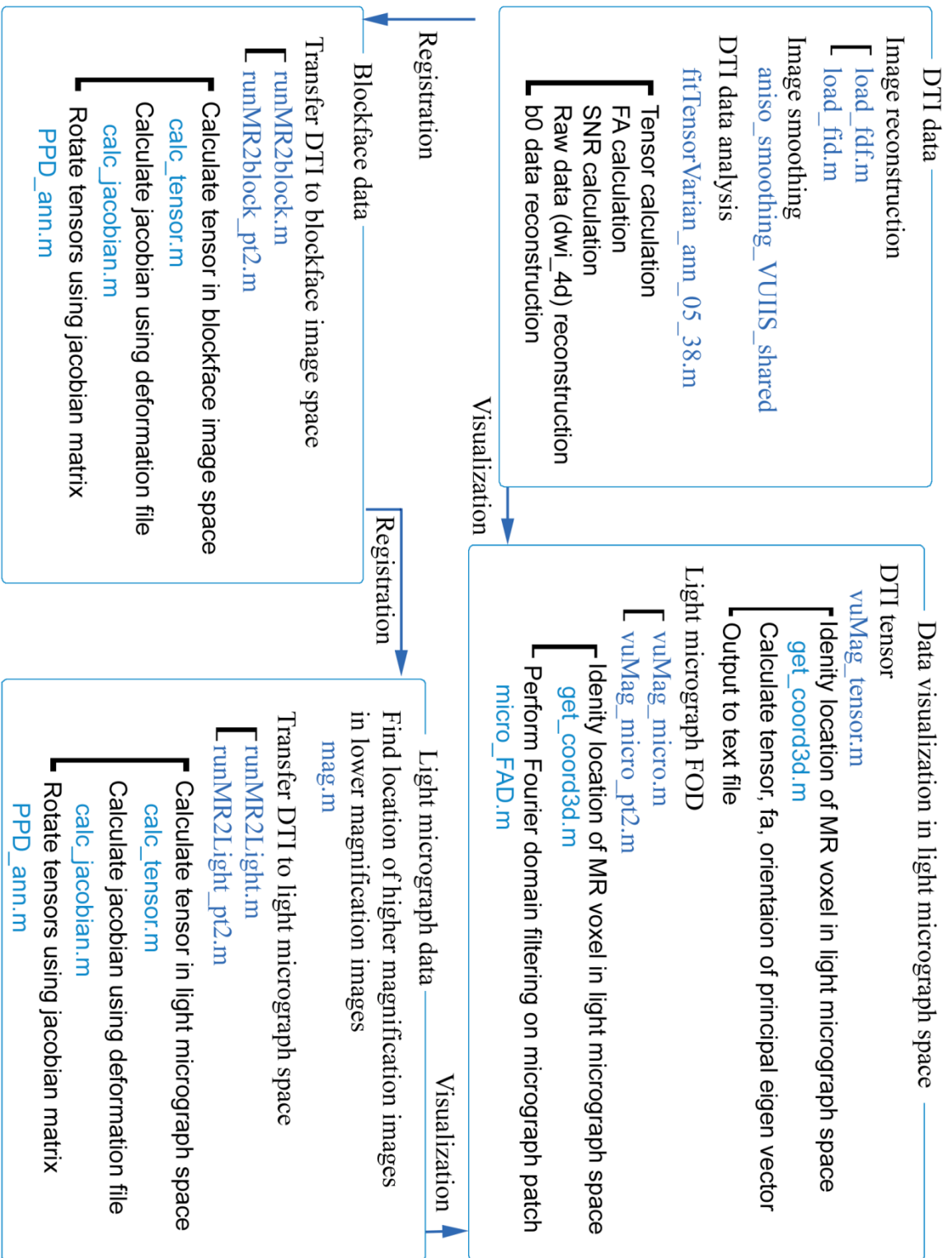
Figure 22. Flow chart of list of programs used. The names of the functions (in blue) that were used to construct, process, and analyze data sets are laid out as a flowchart, categorized according to the related data sets.

REFERENCES

1.   Pierpaoli C, Jezzard P, Basser PJ, Barnett A, Di Chiro G. Diffusion tensor MR imaging of the human brain. Radiology 1996;201(3):637-648.

2.   Basser PJ, Pierpaoli C. Microstructural and physiological features of tissues elucidated by quantitative-diffusion-tensor MRI. J Magn Reson B 1996;111(3):209-219.

3.   Huppi PS, Maier SE, Peled S, Zientara GP, Barnes PD, Jolesz FA, Volpe JJ. Microstructural development of human newborn cerebral white matter assessed in vivo by diffusion tensor magnetic resonance imaging. Pediatr Res 1998;44(4):584-590.

4.   Albers GW, Lansberg MG, Norbash AM, Tong DC, O'Brien MW, Woolfenden AR, Marks MP, Moseley ME. Yield of diffusion-weighted MRI for detection of potentially relevant findings in stroke patients. Neurology 2000;54(8):1562-1567.

5.   Mukherjee P, Bahn MM, McKinstry RC, Shimony JS, Cull TS, Akbudak E, Snyder AZ, Conturo TE. Differences between gray matter and white matter water diffusion in stroke: diffusion-tensor MR imaging in 12 patients. Radiology 2000;215(1):211-220.

6.   Kaufman JA, Ahrens ET, Laidlaw DH, Zhang S, Allman JM. Anatomical analysis of an aye-aye brain (Daubentonia madagascariensis, primates: Prosimii) combining histology, structural magnetic resonance imaging, and diffusion-tensor imaging. Anat Rec A Discov Mol Cell Evol Biol 2005;287(1):1026-1037.

7.   Sun SW, Neil JJ, Liang HF, He YY, Schmidt RE, Hsu CY, Song SK. Formalin fixation alters water diffusion coefficient magnitude but not anisotropy in infarcted brain. Magn Reson Med 2005;53(6):1447-1451.

8.   Hahn EL. Spin echo. Phys Rev 1950;80:580-594.

9.   Carr HY, Purcell EM. Effects of diffusion on free precession in nuclear magnetic resonance experiments. Phys Rev 1954;80:630–638.

10.   Stejskal EO, Tanner JE. Spin Diffusion Measurements: Spin Echoes in the

Presence of a Time-Dependent Field Gradient. J Chem Phys 1965;42(1):288-292.

11. Taylor DG, Bushell MC. The spatial mapping of translational diffusion coefficients by the NMR imaging technique. Phys Med Biol 1985;30(4):345-349.

12. Basser PJ, Mattiello J, LeBihan D. Estimation of the effective self-diffusion tensor from the NMR spin echo. J Magn Reson B 1994;103(3):247-254.

13. Lim KO, Hedehus M, Moseley M, de Crespigny A, Sullivan EV, Pfefferbaum A. Compromised white matter tract integrity in schizophrenia inferred from diffusion tensor imaging. Arch Gen Psychiatry 1999;56(4):367-374.

14. Langevin P. An introduction to stochastic processes in physics: The John Hopkins University Press; 2002.

15. Le Bihan D, Mangin JF, Poupon C, Clark CA, Pappata S, Molko N, Chabriat H. Diffusion tensor imaging: concepts and applications. J Magn Reson Imaging 2001;13(4):534-546.

16. Pierpaoli C, Basser PJ. Toward a quantitative assessment of diffusion anisotropy. Magn Reson Med 1996;36(6):893-906.

17. Ding Z, Gore JC, Anderson AW. Reduction of noise in diffusion tensor images using anisotropic smoothing. Magn Reson Med 2005;53(2):485-490.

18. Weickert J. Coherence-enhancing diffusion filtering. Int J Comput Vis 1999;31:111–127.

19. Basser PJ, Mattiello J, LeBihan D. MR diffusion tensor spectroscopy and imaging. Biophys J 1994;66(1):259-267.

20. Thorpe JA. Elementary topics in differential geometry. New York: Springer-Verlag; 1979.

21. Tuch DS, Weisskoff RM, Belliveau JW, Wedeen VJ. High angular resolution diffusion imaging of the human brain. 1999; Philadelphia. p 321.

22. Makris N, Worth AJ, Sorensen AG, Papadimitriou GM, Wu O, Reese TG, Wedeen

VJ, Davis TL, Stakes JW, Caviness VS, Kaplan E, Rosen BR, Pandya DN, Kennedy DN. Morphometry of in vivo human white matter association pathways with diffusion-weighted magnetic resonance imaging. Ann Neurol 1997;42(6):951-962.

23. Pajevic S, Pierpaoli C. Color schemes to represent the orientation of anisotropic tissues from diffusion tensor data: application to white matter fiber tract mapping in the human brain. Magn Reson Med 1999;42(3):526-540.

24. Blum F. Notiz uber die anwendung des formaldehyds (formol) als harrungs-und koservierungsmittel. Anat Anz 1894;9:229.

25. Hopwood D. The reactions between formaldehyde, glutaraldehyde and osmium tetroxide, and their fixation effects o bovine serum albumin and on tissue blocks. Histochemie 1970;24(1):50-64.

26. Underhill BML. The rate of penetration of fixatives. J R Microsc Soc 1932;52:113.

27. Durgun-Yucel B, Hopwood D, Yucel AH. The effects of mercaptoethanol-formaldehyde on tissue fixation and protein retention. Histochem J 1996;28(5):375-383.

28. Fox CH, Johnson FB, Whiting J, Roller PP. Formaldehyde fixation. J Histochem Cytochem 1985;33(8):845-853.

29. Bancroft JD, Cook HC. Manual of Histological Techniques and their Diagnositic Application. Edinburgh; New York Churchill Livingstone; 1994. 349-356 p.

30. Gallyas F. Silver staining of myelin by means of physical development. Neurol Res 1979;1(2):203-209.

31. Press WH. Numerical Recipes in C. Cambridge, U.K.: Cambridge Univ. Press; 1992. 412–419 p.

32. Maes F, Collignon A, Vandermeulen D, Marchal G, Suetens P. Multimodality image registration by maximization of mutual information. IEEE Trans Med Imaging 1997;16(2):187-198.

33.   Shannon CE. A mathematical theory of communication. Bell System Technical Journal 1948;27:379-423.

34.   Rauschning W. Surface cryoplaning. A technique for clinical anatomical correlations. Upsala journal of medical sciences 1986;91(3):251-255.

35.   Toga AW, Ambach KL, Schluender S. High-resolution anatomy from in situ human brain. NeuroImage 1994;1(4):334-344.

36.   Chakravarty MM, Bertrand G, Hodge CP, Sadikot AF, Collins DL. The creation of a brain atlas for image guided neurosurgery using serial histological data. NeuroImage 2006;30(2):359-376.

37.   Ho PS, Yu SW, Sether L, Wagner M, Haughton VM. MR and cryomicrotomy of C1 and C2 roots. Ajnr 1988;9(5):829-831.

38.   Dauguet J, Delzescaux T, Conde F, Mangin JF, Ayache N, Hantraye P, Frouin V. Three-dimensional reconstruction of stained histological slices and 3D non-linear registration with in-vivo MRI for whole baboon brain. Journal of neuroscience methods 2007;164(1):191-204.

39.   Palm C, Axer M, Grassel D, Dammers J, Lindemeyer J, Zilles K, Pietrzyk U, Amunts K. Towards Ultra-High Resolution Fibre Tract Mapping of the Human Brain - Registration of Polarised Light Images and Reorientation of Fibre Vectors. Frontiers in human neuroscience 2010;4:9.

40.   Scholtes F, Phan-Ba R, Theunissen E, Adriaensens P, Brook G, Franzen R, Bouhy D, Gelan J, Martin D, Schoenen J. Rapid, postmortem 9.4 T MRI of spinal cord injury: correlation with histology and survival times. Journal of neuroscience methods 2008;174(2):157-167.

41.   Engelhorn T, Eyupoglu IY, Schwarz MA, Karolczak M, Bruenner H, Struffert T, Kalender W, Doerfler A. In vivo micro-CT imaging of rat brain glioma: a comparison with 3T MRI and histology. Neuroscience letters 2009;458(1):28-31.

42.   Grate LL, Golden JA, Hoopes PJ, Hunter JV, Duhaime AC. Traumatic brain injury in piglets of different ages: techniques for lesion analysis using histology and magnetic resonance imaging. Journal of neuroscience methods 2003;123(2):201-206.

43.   Ma B, Lin Z, Winkelbach S, Lindenmaier W, Dittmar KE. Automatic registration of serial sections of mouse lymph node by using Image-Reg. Micron 2008;39(4):387-396.

44.   Breen MS, Lancaster TL, Wilson DL. Correcting spatial distortion in histological images. Comput Med Imaging Graph 2005;29(6):405-417.

45.   Pitiot A, Bardinet E, Thompson PM, Malandain G. Piecewise affine registration of biological images for volume reconstruction. Medical image analysis 2006;10(3):465-483.

46.   Lu Y, Aldroubi A, Gore JC, Anderson AW, Ding Z. Improved fiber tractography with Bayesian tensor regularization. NeuroImage 2006;31(3):1061-1074.

47.   Peled S, Friman O, Jolesz F, Westin CF. Geometrically constrained two-tensor model for crossing tracts in DWI. Magnetic resonance imaging 2006;24(9):1263-1270.

48.   Chen B, Song AW. Diffusion tensor imaging fiber tracking with local tissue property sensitivity: phantom and in vivo validation. Magnetic resonance imaging 2007.

49.   Lin CP, Wedeen VJ, Chen JH, Yao C, Tseng WY. Validation of diffusion spectrum magnetic resonance imaging with manganese-enhanced rat optic tracts and ex vivo phantoms. Neuroimage 2003;19(3):482-495.

50.   Perrin M, Poupon C, Rieul B, Leroux P, Constantinesco A, Mangin JF, Lebihan D. Validation of q-ball imaging with a diffusion fibre-crossing phantom on a clinical scanner. Philos Trans R Soc Lond B Biol Sci 2005;360(1457):881-891.

51.   Watanabe M, Aoki S, Masutani Y, Abe O, Hayashi N, Masumoto T, Mori H, Kabasawa H, Ohtomo K. Flexible ex vivo phantoms for validation of diffusion tensor tractography on a clinical scanner. Radiat Med 2006;24(9):605-609.

52.   Pullens P, Roebroeck A, Goebel R. Ground truth hardware phantoms for validation of diffusion-weighted MRI applications. J Magn Reson Imaging 2010;32(2):482-488.

53.   Lin CP, Tseng WY, Cheng HC, Chen JH. Validation of diffusion tensor magnetic

resonance axonal fiber imaging with registered manganese-enhanced optic tracts. NeuroImage 2001;14(5):1035-1047.

54.   D'Arceuil HE, Westmoreland S, de Crespigny AJ. An approach to high resolution diffusion tensor imaging in fixed primate brain. NeuroImage 2007;35(2):553-565.

55.   D'Arceuil H, de Crespigny A. The effects of brain tissue decomposition on diffusion tensor imaging and tractography. NeuroImage 2007;36(1):64-68.

56.   Schmahmann JD, Pandya DN, Wang R, Dai G, D'Arceuil HE, de Crespigny AJ, Wedeen VJ. Association fibre pathways of the brain: parallel observations from diffusion spectrum imaging and autoradiography. Brain 2007;130(Pt 3):630-653.

57.   Cowan WM, Gottlieb DI, Hendrickson AE, Price JL, Woolsey TA. The autoradiographic demonstration of axonal connections in the central nervous system. Brain research 1972;37(1):21-51.

58.   Schmahmann JD, Pandya DN. Fiber pathways of the brain. New York: Oxford University Press; 2006. 654 p.

59.   Dauguet J, Peled S, Berezovskii V, Delzescaux T, Warfield SK, Born R, Westin CF. Comparison of fiber tracts derived from in-vivo DTI tractography with 3D histological neural tract tracer reconstruction on a macaque brain. NeuroImage 2007.

60.   Leergaard TB, White NS, de Crespigny A, Bolstad I, D'Arceuil H, Bjaalie JG, Dale AM. Quantitative histological validation of diffusion MRI fiber orientation distributions in the rat brain. PloS one 2010;5(1):e8595.

61.   Schmierer K, Wheeler-Kingshott CA, Boulby PA, Scaravilli F, Altmann DR, Barker GJ, Tofts PS, Miller DH. Diffusion tensor imaging of post mortem multiple sclerosis brain. NeuroImage 2007;35(2):467-477.

62.   Hsu EW, Muzikant AL, Matulevicius SA, Penland RC, Henriquez CS. Magnetic resonance myocardial fiber-orientation mapping with direct histological correlation. Am J Physiol 1998;274(5 Pt 2):H1627-1634.

63.   Scollan DF, Holmes A, Winslow R, Forder J. Histological validation of myocardial microstructure obtained from diffusion tensor magnetic resonance

imaging. Am J Physiol 1998;275(6 Pt 2):H2308-2318.

64.   Holmes AA, Scollan DF, Winslow RL. Direct histological validation of diffusion tensor MRI in formaldehyde-fixed myocardium. Magn Reson Med 2000;44(1):157-161.

65.   Damon BM, Ding Z, Anderson AW, Freyer AS, Gore JC. Validation of diffusion tensor MRI-based muscle fiber tracking. Magn Reson Med 2002;48(1):97-104.

66.   Smith SM. Fast robust automated brain extraction. Human brain mapping 2002;17(3):143-155.

67.   Li R. Automatic Placement of regions of interest in medical images using image registration [Master's Thesis]. Nashville: Vanderbilt University; 2001.

68.   Rohde GK, Aldroubi A, Dawant BM. The adaptive bases algorithm for intensity-based nonrigid image registration. IEEE Trans Med Imaging 2003;22(11):1470-1479.

69.   Besl PJ, McKay HD. A method for registration of 3-D shapes. IEEE Trans Pattern Anal Mach Intell 1992;14(2):239 - 256.

70.   Fitzpatrick JM, Hill DL, Maurer CR. Handbook of Medical Imaging. In: Fitzpatrick JM, Sonka M, editors. Medical Image Processing and Analysis. Volume 2. Bellingham, Washington: SPIE International Society for Optical Engineering; 2000. p 447-513.

71.   Sinha TK, Khatib-Shahidi S, Yankeelov TE, Mapara K, Ehtesham M, Cornett DS, Dawant BM, Caprioli RM, Gore JC. Integrating spatially resolved three-dimensional MALDI IMS with in vivo magnetic resonance imaging. Nature methods 2008;5(1):57-59.

72.   Khatib-Shahidi S, Andersson M, Herman JL, Gillespie TA, Caprioli RM. Direct molecular analysis of whole-body animal tissue sections by imaging MALDI mass spectrometry. Analytical chemistry 2006;78(18):6448-6456.

73.   Li X, Yankeelov TE, Rosen GD, Gore JC, Dawant BM. Enhancement of histological volumes through averaging and their use for the analysis of magnetic resonance images. Magn Reson Imaging 2009;27(3):401-416.

74.   Rosen GD. MBL Training Manual - Detailed Protocol. Volume 2010; 2003.

75.   Pierpaoli C, Barnett A, Pajevic S, Chen R, Penix LR, Virta A, Basser P. Water diffusion changes in Wallerian degeneration and their dependence on white matter architecture. NeuroImage 2001;13(6 Pt 1):1174-1185.

76.   Fellgiebel A, Wille P, Muller MJ, Winterer G, Scheurich A, Vucurevic G, Schmidt LG, Stoeter P. Ultrastructural hippocampal and white matter alterations in mild cognitive impairment: a diffusion tensor imaging study. Dement Geriatr Cogn Disord 2004;18(1):101-108.

77.   Roberts TP, Liu F, Kassner A, Mori S, Guha A. Fiber density index correlates with reduced fractional anisotropy in white matter of patients with glioblastoma. AJNR Am J Neuroradiol 2005;26(9):2183-2186.

78.   Warner TD, Behnke M, Eyler FD, Padgett K, Leonard C, Hou W, Garvan CW, Schmalfuss IM, Blackband SJ. Diffusion tensor imaging of frontal white matter and executive functioning in cocaine-exposed children. Pediatrics 2006;118(5):2014-2024.

79.   Stahl R, Dietrich O, Teipel SJ, Hampel H, Reiser MF, Schoenberg SO. White matter damage in Alzheimer disease and mild cognitive impairment: assessment with diffusion-tensor MR imaging and parallel imaging techniques. Radiology 2007;243(2):483-492.

80.   Foong J, Symms MR, Barker GJ, Maier M, Miller DH, Ron MA. Investigating regional white matter in schizophrenia using diffusion tensor imaging. Neuroreport 2002;13(3):333-336.

81.   Naggara O, Oppenheim C, Rieu D, Raoux N, Rodrigo S, Dalla Barba G, Meder JF. Diffusion tensor imaging in early Alzheimer's disease. Psychiatry Res 2006;146(3):243-249.

82.   Rose SE, McMahon KL, Janke AL, O'Dowd B, de Zubicaray G, Strudwick MW, Chalk JB. Diffusion indices on magnetic resonance imaging and neuropsychological performance in amnestic mild cognitive impairment. J Neurol Neurosurg Psychiatry 2006;77(10):1122-1128.

83.   Conturo TE, Lori NF, Cull TS, Akbudak E, Snyder AZ, Shimony JS, McKinstry RC, Burton H, Raichle ME. Tracking neuronal fiber pathways in the living human

brain. Proc Natl Acad Sci U S A 1999;96(18):10422-10427.

84. Basser PJ, Pajevic S, Pierpaoli C, Duda J, Aldroubi A. In vivo fiber tractography using DT-MRI data. Magn Reson Med 2000;44(4):625-632.

85. Berman JI, Mukherjee P, Partridge SC, Miller SP, Ferriero DM, Barkovich AJ, Vigneron DB, Henry RG. Quantitative diffusion tensor MRI fiber tractography of sensorimotor white matter development in premature infants. NeuroImage 2005;27(4):862-871.

86. Catani M. Diffusion tensor magnetic resonance imaging tractography in cognitive disorders. Curr Opin Neurol 2006;19(6):599-606.

87. Alexander AL, Hasan KM, Lazar M, Tsuruda JS, Parker DL. Analysis of partial volume effects in diffusion-tensor MRI. Magn Reson Med 2001;45(5):770-780.

88. Basser PJ, Pajevic S. Statistical artifacts in diffusion tensor MRI (DT-MRI) caused by background noise. Magn Reson Med 2000;44(1):41-50.

89. Anderson AW. Theoretical analysis of the effects of noise on diffusion tensor imaging. Magn Reson Med 2001;46(6):1174-1188.

90. Jeong HK, Anderson AW. Characterizing fiber directional uncertainty in diffusion tensor MRI. Magn Reson Med 2008;60(6):1408-1421.

91. Koay CG, Nevo U, Chang LC, Pierpaoli C, Basser PJ. The elliptical cone of uncertainty and its normalized measures in diffusion tensor imaging. IEEE Trans Med Imaging 2008;27(6):834-846.

92. Lazar M, Alexander AL. An error analysis of white matter tractography methods: synthetic diffusion tensor field simulations. NeuroImage 2003;20(2):1140-1153.

93. Chen B, Song AW. Diffusion tensor imaging fiber tracking with local tissue property sensitivity: phantom and in vivo validation. Magnetic resonance imaging 2008;26(1):103-108.

94. Dauguet J, Peled S, Berezovskii V, Delzescaux T, Warfield SK, Born R, Westin CF. Comparison of fiber tracts derived from in-vivo DTI tractography with 3D

histological neural tract tracer reconstruction on a macaque brain. NeuroImage 2007;37(2):530-538.

95.   Alexander DC, Pierpaoli C, Basser PJ, Gee JC. Spatial transformations of diffusion tensor magnetic resonance images. IEEE Trans Med Imaging 2001;20(11):1131-1139.

96.   Chaudhuri S, Nguyen H, Rangayyan RM, Walsh S, Frank CB. A Fourier domain directional filtering method for analysis of collagen alignment in ligaments. IEEE Transactions on Biomedical Engineering 1987;34(7):509-518.